A Modelling Framework for Simulation of Ultrasonic Guided Wave-Based Inspection of Welded Rail Tracks

Dineo A. Ramatlo[1], Craig S. Long[2], Philip W. Loveday[3] and Daniel N. Wilke[1]

[1] *University of Pretoria, South Africa*

[2] *CSIR Manufacturing Cluster, South Africa*

[3] *University of the Witwatersrand, South Africa*

Abstract

A modelling framework for ultrasonic inspection of waveguides with arbitrary discontinuities, excited using piezoelectric transducers, is developed. The framework accounts for multi-modal, dispersive and damped one dimensional propagation over long distances. The proposed model is applied to simulate a realistic guided wave-based inspection of a welded rail. The framework models the excitation, propagation and scattering of guided waves from welds by respectively employing a hybrid model that couples a 3D FEM model of a piezoelectric transducer with a 2D SAFE model of the rail; a 2D SAFE model of the rail; and another hybrid method which couples a 3D FEM model of the arbitrary discontinuity (weld) with two SAFE models of the rail to represent the semi-infinite incoming and outgoing waveguides. Optimal damping parameters for hysteretic and viscous damping, respectively, are determined using a model updating procedure to approximate attenuation in the rail. Good agreement between the experimental measurement and simulation is demonstrated, even for weld reflections originating over 640m from the transducer location. The proposed physics-based framework can be used to efficiently perform multiple analyses considering different numbers and locations of welds, different excitation signals or to investigate the effects of changes in parameters such as transducer geometry, or material property variations caused by temperature fluctuations. The framework could therefore be used in future to set up a digital twin of a section of rail track, or in the development of a rail monitoring system by predicting reflections from defects which cannot readily be measured, but which can be simulated.

Keywords: Guided wave ultrasound; Welded rail; Hybrid SAFE method; Piezoelectric transducer;

1. Introduction

The use of Guided Wave Ultrasound (GWU) for Non-Destructive Evaluation (NDE) and structural health monitoring is receiving significant research attention. This is because GWU has demonstrated the potential for inspection or monitoring of structures which act as waveguides for elastic waves such as plates, pipes and railway tracks [1, 2, 3]. One of the attractive properties of GWU is the ability to interrogate or monitor large volumes of a structure from a single transducer location, especially when compared with the conventional ultrasonic inspection. This feature is exploited in a permanent monitoring system for railway tracks which is currently being used to monitor a heavy haul line in South Africa [4, 5]. GWU-based NDE systems can be designed to distinguish benign structural features from defects, using knowledge of how modes interact with different geometrical features. Furthermore, GWU can be used to inspect or monitor the structural health of inaccessible parts of structures, such as insulated or buried pipes [6, 7].

The design of GWU-based NDE systems is, however, complicated by the presence of multiple propagating modes and the dispersive nature of these modes, especially when long-range propagation is involved. For this reason, the development of GWU systems usually requires the use of mathematical modelling. Modelling can be used to design transducers to preferentially excite desired modes, offering insights into how the location and dynamics of a transducer influence the excitation of guided wave modes. It can also be used to predict and analyse the dispersion and attenuation of propagating modes, required to develop signal processing strategies. Finally, modelling is also necessary to simulate the very complex scattering of propagating modes from discontinuities such as structural features or defects.

The traditional 3D Finite Element Method (FEM) with an explicit time-domain solver could be adopted to simulate the excitation, propagation and scattering of GWU if relatively short sections of waveguides are considered [8, 9, 10]. The work in [8] does apply specifically to a rail problem; however, the fine temporal and spatial discretization required at frequencies employed in GWU-based rail monitoring systems and the propagation distances achieved (kilometres in some cases) makes explicit solvers impractical for modelling the entire rail section. To date, only a few authors have reported the implementation of numerical models to simulate a complete guided wave-based inspection.

Jezzine et al. [11] developed a model to simulate guided wave-based inspection with a transducer mounted at the end of a semi-finite 1D waveguide. In this model the energy propagates in one direction only, making this model inappropriate for long, continuous waveguides such as pipelines and rails. For these applications transducers are generally attached to the circumference of the waveguide, and an inspection is carried out in both directions. Furthermore, in [11] the transducer is modelled simply as a source of normal stresses, and transducer dynamics are not taken into account. Loveday [12] developed a hybrid method to simulate wave propagation excited by a piezoelectric transducer attached to a waveguide, accounting for transducer dynamics. This method couples a 3D FEM model of a piezoelectric transducer with a 2D Semi-Analytical Finite Element (SAFE) model of the elastic waveguide. The method has been refined, verified and employed to design and optimize resonant piezoelectric transducers for targeting specific propagating modes in rails [13, 14].

Furthermore, Jezzine et al. [11] considered only transverse cracks modelled using a SAFE-based [15, 16] analysis. Baronian and co-workers [17, 18] have developed a method to compute scattering from more general structural features and defects with complex geometry. This method has been implemented in the analysis software, CIVA [19]. Benmeddour et al. [20] introduced a hybrid method which uses a 3D FEM model of an arbitrary discontinuity and SAFE models to represent the semi-infinite incoming and outgoing waveguides. This method was used to predict reflection amplitudes from discontinuities in rails such as aluminothermic welds and defects such as cracks [3, 21], indicating that it should be possible to detect defects in rails at long-range before complete breaks occur [3]. Baronian et al. [22] demonstrated the application of the CIVA software to simulate an inspection with multiple local discontinuities. The scattering matrices for the coupled local discontinuities were computed by considering the scattering from respective discontinuities and the propagation between them. The method was successfully applied for short-range propagation (less than tens of metres) where a relatively short time signal was required. This approach could be adopted for long-range propagation (over hundreds of metres) but the effects of attenuation and dispersion in the time domain would need to be accounted for.

Although numerical modelling is a useful tool for the prediction and analysis of wave propagation, practical GWU-based monitoring systems contain variations which cannot easily be simulated. When considering rail track, some environmental operating conditions (EOCs) can be accounted for; for example, temperature, rail tension effects, and wear [23]. Other effects, however, are far more complex and difficult to model, for example, effects of passing trains, rail track sinking into the ballast, scattering from metal clips securing the rail, and various others. These effects introduce time-varying coherent noise into measured GWU signals, which potentially obscure small defect signatures.

To overcome these issues for pipe monitoring systems, Liu et al. [24] proposed a method to quantify the system performance in the presence of realistic EOCs. The scheme effectively combines the complex measured signals from benign structural features accounting for EOCs, and simulated defect signals. For rail monitoring systems, access to realistic measured defect signals is challenging since laboratory experiments introducing defects are not possible due to the long-range propagation and defects in operational rail are repaired as soon as they are detected. Therefore, this simple but powerful idea would allow researchers to estimate performance measures which would otherwise be very difficult or indeed impossible to estimate.

The accuracy of the proposed procedure is, of course, dependant on the accuracy of the simulated defect signature. For rail monitoring applications, there are unique challenges which require consideration when compared to other monitoring systems. In the pipe monitoring system, an array of transducers is used to transmit and receive only the torsional mode of the pipe which has negligible dispersion. In the case of rail monitoring, the system will probably employ an array of only a few transducers, and therefore multiple modes of propagation will be transmitted and received. These modes are generally dispersive, and this must be taken into account as long distances (thousands of metres) are involved. Also, the various modes of propagation attenuate differently due to damping introduced by the rail support.

Table 1: A summary of related research with their underlying physics and modelling considerations, which is compared to the consolidated single modelling framework proposed in this study.

Reference	Excitation	Propagation			Scattering		Validation
	Transducer Physics & Dynamics	Attenuation	Dispersion Effects	Long-range ($\gg 100\,m$)	Discontinuities	Multiple Discontinuities	Experimental Measurement
[8, 9, 10] Explicit solver	Point forces		Low		Transverse defect/end reflections		
[11]	Normal pressure		Low		Transverse crack		
[17, 18]	Normal pressure		Low		Arbitrary damage ✓		
[22]	Normal pressure		Low		Arbitrary damage ✓	✓	
Modelling aspects consolidated into a single modelling framework	Resonant Transducer [12, 13, 14] ✓	Derived from experimental measure-ments ✓	Large ✓	✓	Arbitrary damage /welds [3, 20, 21] ✓	✓	✓

The aim of this paper is, therefore, to develop a modelling framework to simulate guided wave-based inspection of a welded rail using piezoelectric transducers. The novelty of the paper lies in demonstrating the simulation of an inspection where relevant modelling aspects which were separately considered in the previous literature are now consolidated into a single modelling framework as summarized in Table 1. As outlined, other researchers have simulated guided wave-based inspections in environments where propagation is over a relatively short distance (less than tens of meters), and the effects of attenuation and dispersion are very low. These authors excited the guided waves by employing simple nodal forces [8, 9, 10] or a normal pressure [11, 17, 18, 22] and inspection was carried out only on one side of the source, ignoring reflections from the opposite direction. The contributions of this paper are therefore to (1) simulate guided wave-based inspection in both directions from a single transducer source, (2) combine models of a resonant transducer and multiple discontinuities to simulate a long-range inspection (hundreds of meters) while accounting for attenuation and dispersion, and (3) validate the simulated inspection using the experimental measurement from an operational railway line.

Since experimental measurements containing real defect signatures are not available, reflections from available discontinuities on operational rail, specifically aluminothermic welds, will be used to evaluate the accuracy of the proposed procedure. This novel framework effectively represents a procedure to initialise a digital twin of a physical inspection setup by combining realistic models of excitation, propagation and scattering of GWU, as shown in Figure 1. For this study, a digital twin refers to a digital replica of a physical inspection system. The process of building a digital twin involves first setting up a digital model and after that collecting operational data from a physical inspection system. Data is then transferred to the digital model, to improve and evolve the digital inspection model. This process is illustrated in Figure 2. The focus of this paper is on the first step, which is to setup a digital model of a GWU-based inspection system. In future, the digital twin modelling framework will be employed to improve available inspection systems and also to design new inspection systems. Furthermore, the digital twin could be employed to model unavailable damage scenarios.

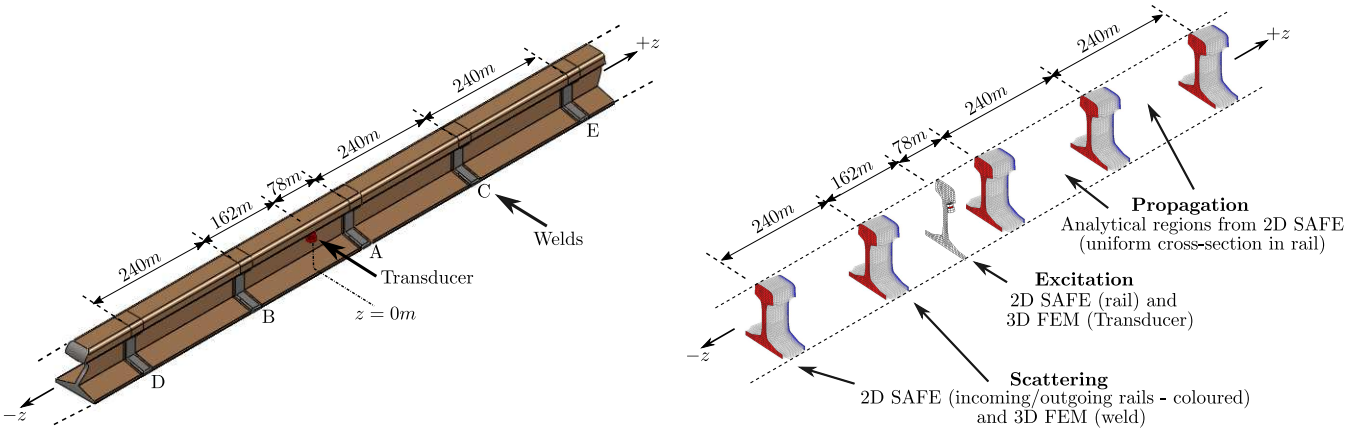

(a) Section of a welded rail from the field.

(b) Modelling of guided wave excitation, propagation and scattering in welded rails.

Figure 1: Proposed model of a physical inspection setup combining realistic models of the excitation, propagation and scattering of GWU.

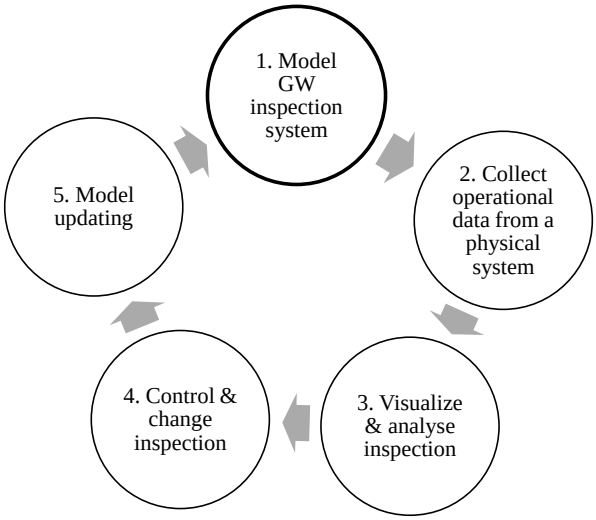

Figure 2: The process of building a digital twin [25].

It is believed that if the proposed procedure can accurately simulate reflections from welds, then it will also be capable of modelling the reflections from defects. In future, these simulated defect signatures can then be superimposed on measured data for the evaluation of a monitoring system. As the proposed procedure represents a physics-based simulation, it will be possible to modify input parameters to account for the influence of environmental factors such as temperature. Furthermore, since a transducer model is included, system-level evaluations, including evaluating the ability of different transducer arrays to detect various defect types, will be possible. Unlike 3D FEM models, signals from reflectors can easily be isolated, allowing the reflections from a defect to be isolated even from reflectors close by, as in the case of a defect close to a weld. The proposed model of a section of rail track can also be used to interpret changes that are observed in the experimental signals and to develop compensation techniques to mitigate the influence of these changes on the performance of the monitoring system.

The techniques used to model the various elements of GWU in rails are described in Section 2. Section 3

describes a guided wave-based inspection on a section of rail track and presents the situation to be modelled and provides the experimental result. The simulation of the inspection is described in Section 4, where the different elements are combined to produce the simulation results presented in Section 5. The simulation results are validated using an experimental measurement from an operational rail in Section 5 and conclusions are drawn in Section 6.

2. Guided Wave Modelling

This paper presents a framework in which several existing numerical models are used in combination to effectively create a numerical representation of a guided wave-based inspection system for rail, as depicted in Figure 1. The system includes a piezoelectric transducer to excite propagating waves in the rail which acts as a waveguide and aluminothermic welds which act as reflectors of the propagating waves. This section presents a summary of the numerical models which form the basis of the proposed modelling framework presented in detail in Section 4. The SAFE method for modelling wave propagation is explained first, followed by the two hybrid methods for modelling the excitation and the scattering of guided waves from discontinuities, respectively. Since these methods are presented in detail elsewhere, only the salient points of each method will be presented here.

2.1. The Semi-Analytical Finite Element Method

The semi-analytical finite element (SAFE) method for 1D propagation uses an analytic treatment for variations in the propagation direction and a discretized representation to describe variations in the cross-section. In this case, we consider an infinite elastic waveguide with an arbitrary but constant cross-section in the $x-y$ plane. For wave propagation in the $z-$direction, the time-varying displacement vector $\mathbf{U}$ is expressed in complex exponential form as:

$$\mathbf{U}(x,y,z,t) = [u_x(x,y),\ u_y(x,y),\ u_z(x,y)]^T e^{-j(\kappa z - \omega t)} \tag{1}$$

where u_x, u_y and u_z represent the displacements in the $x-, y-$ and $z-$directions respectively, κ is the wavenumber and ω is the circular frequency [15]. A transformation of the displacements from a physical coordinate system to a SAFE coordinate system is convenient to ensure that symmetric stiffness matrices result [16, 26]. We employ the proposal of Damljanović and Weaver [26] and define:

$$\mathbf{U} = \mathbf{T}\bar{\mathbf{U}} \tag{2}$$

where the transformation matrix $\mathbf{T}$, is given by

$$\mathbf{T} = \begin{bmatrix} 1 & 0 & 0 \\ 0 & 1 & 0 \\ 0 & 0 & j \end{bmatrix} \tag{3}$$

The transformation from SAFE coordinates to physical coordinates is similarly given by:

$$\bar{\mathbf{U}} = \mathbf{T}^{*T}\mathbf{U} \tag{4}$$

where $(\cdot)^{*T}$ represents the complex conjugate transpose. For convenience, the remainder of this section will present quantities in the physical coordinates since similar transformations are possible for all vector and tensor properties.

2.1.1. Solution of the Free Vibration Problem

At a specific circular frequency ω, the mode shapes, as well as wavenumbers associated with each mode, can be computed by solving the eigenvalue problem [13]:

$$[\mathbf{A} - \kappa_i \mathbf{B}]\{\mathbf{\Psi}_i\} = \{\mathbf{0}\}, \text{ with } \mathbf{\Psi}_i = \begin{Bmatrix} \boldsymbol{\psi}_i \\ \kappa_i \boldsymbol{\psi}_i \end{Bmatrix} \tag{5}$$

and where $\mathbf{A}$ and $\mathbf{B}$ are matrices consisting of SAFE mass and stiffness matrices.

$$\mathbf{A} = \begin{bmatrix} \mathbf{K}_0 - \omega^2\mathbf{M} & \mathbf{0} \\ \mathbf{0} & -\mathbf{K}_2 \end{bmatrix} \text{ and } \mathbf{B} = \begin{bmatrix} -j\mathbf{K}_1 & -\mathbf{K}_2 \\ -\mathbf{K}_2 & \mathbf{0} \end{bmatrix} \tag{6}$$

Solving Equation (5) results in real, forward and backward propagating modes with wavenumbers $\boldsymbol{\kappa}^+$ and $\boldsymbol{\kappa}^-$, respectively, and associated mode shapes $\boldsymbol{\psi}^+$ and $\boldsymbol{\psi}^-$. Also computed are a number of non-propagating evanescent modes. Finally, for each wavenumber computed $\kappa_i(\omega)$, the phase velocity $v_p(\omega) = \frac{\omega}{\kappa}$ and group velocity $v_g(\omega) = \frac{d\omega}{d\kappa}$ can also be computed. For more detail regarding the implementation, the reader is referred to [13, 16].

A procedure to determine the material and geometric parameters of a worn rail was proposed in [23]. The same section of rail is considered in this work, and the geometry of the worn, non-symmetric UIC60 rail is depicted in Figure 3, discretized using quadratic SAFE elements. Figures 4a-c depicts the frequency-dependent wavenumber, phase velocity and group velocity curves in the frequency range of interest (between $30kHz$ *and* $50kHz$). Modes are numbered based on the strategy presented in [27]. Since the geometry is not symmetric, modes do not cross in the wavenumber-frequency dispersion curves, resulting in several mode repulsions, which can clearly be seen in the group velocity curves [27].

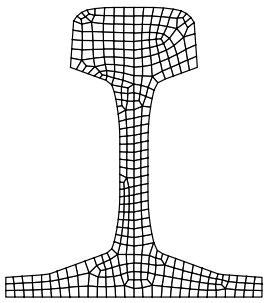

Figure 3: SAFE model of a worn non-symmetric UIC60 rail.

2.1.2. Solution of the Damped Free Vibration Problem

Guided waves attenuate as they propagate due to material damping. In the case of rail track, additional attenuation results due to the track being continuously supported at the foot of the rail, which causes modes with motion in the foot to be attenuated more strongly than modes which do not have energy concentrated in the foot of the rail. A viscous material layer under the rail foot was previously used by Ryue et al. to account for this damping [28].

Bartoli et al. [29] used the Kelvin-Voigt model and a hysteretic model to represent material damping by allowing complex components in the material constitutive matrix relating stresses and strains. Allowing for complex material laws results in a generally complex eigenvalue problem, and therefore the resulting propagating wavenumbers are also complex. This adds complexity when sorting modes and is not convenient for our implementation.

We therefore propose to approximate the complex wavenumbers for a damped waveguide using the modes solved from the real-valued problem without having to solve the eigenvalue problem again. Equation (5) is modified to include a hysteretic damping term proportional to the stiffness and viscous damping under the foot of the rail. The $\mathbf{A}$ and $\mathbf{B}$ matrices in Equation (6) thus become:

$$\tilde{\mathbf{A}} = \begin{bmatrix} (1+j\beta)\mathbf{K}_0 + c(j\tilde{\mathbf{I}}) - \omega^2\mathbf{M} & \mathbf{0} \\ \mathbf{0} & -(1+j\beta)\mathbf{K}_2 \end{bmatrix} \text{ and } \tilde{\mathbf{B}} = \begin{bmatrix} -(1+j\beta)\mathbf{K}_1 & -(1+j\beta)\mathbf{K}_2 \\ -(1+j\beta)\mathbf{K}_2 & \mathbf{0} \end{bmatrix} \tag{7}$$

where β is a proportional hysteretic damping factor added to all degrees of freedom, c is a viscous damping factor, and $\tilde{\mathbf{I}}$ is a modified identity matrix with ones at the foot degrees of freedom of the rail in contact with the supports. The complex wavenumbers for a damped waveguide are then estimated from:

$$\tilde{\kappa}_i \approx \frac{\boldsymbol{\Psi}_i^T \tilde{\mathbf{A}} \boldsymbol{\Psi}_i}{\boldsymbol{\Psi}_i^T \tilde{\mathbf{B}} \boldsymbol{\Psi}_i} \tag{8}$$

where $\mathbf{\Psi}_i$ is the mode shape vector from the undamped problem in Equation (5). This estimate produced accurate results for the damping values considered here since damping is relatively light. The attenuation curves in units of dB/m obtained by multiplying $imag\,(\tilde{\kappa})$ with a factor of -8.686 as suggested by reference [28], are plotted in Figure 4d. The damping parameters employed to approximate the attenuation were obtained from an optimization procedure explained in Section 4.2.3.

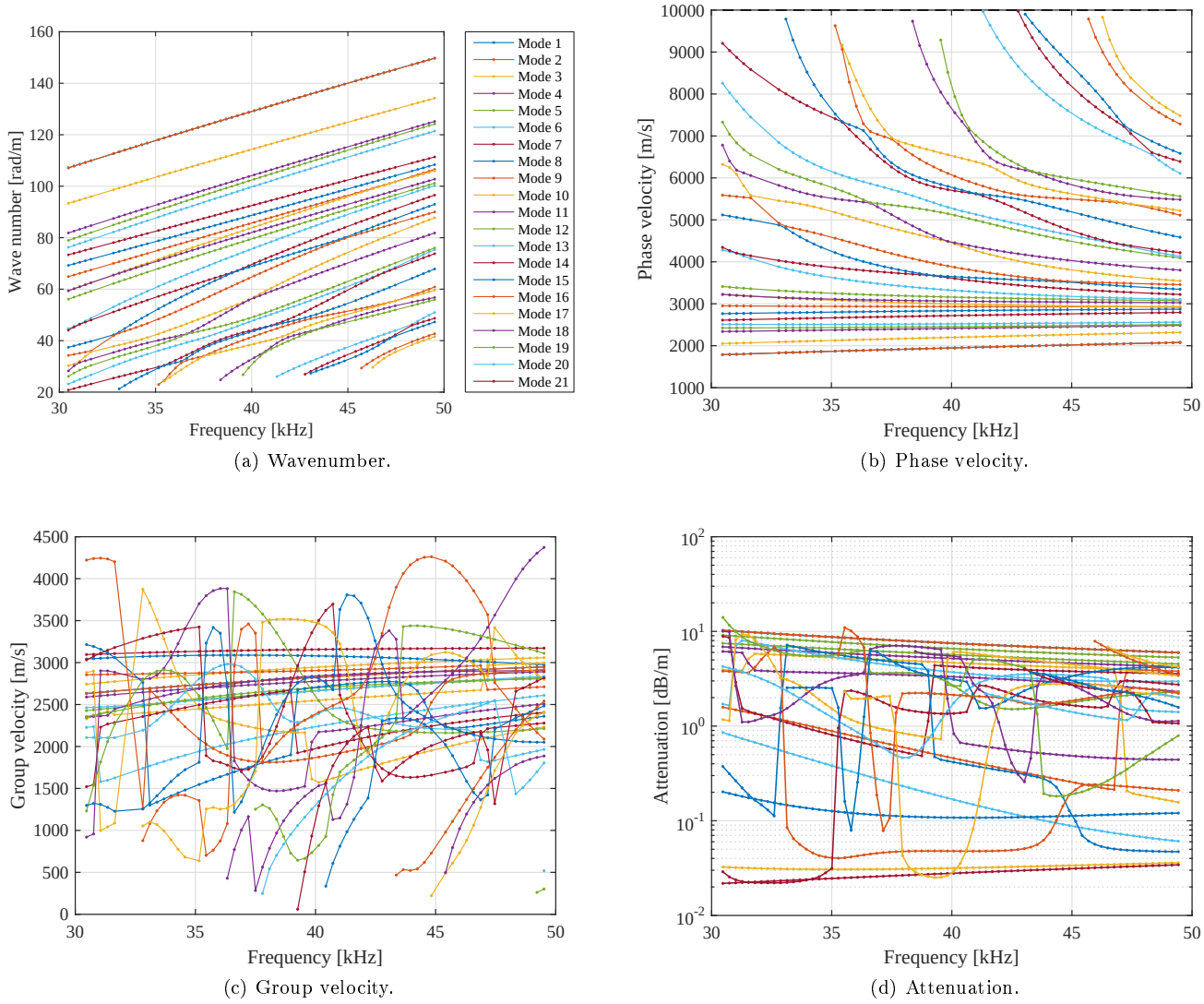

(a) Wavenumber.

(b) Phase velocity.

(c) Group velocity.

(d) Attenuation.

Figure 4: Dispersion properties of UIC60 rail.

2.2. Hybrid SAFE-3D Model for Transducer Excitation

Loveday [12, 30] proposed a method to couple a solid 3D FEM model of a piezoelectric transducer and a 2D SAFE model of an elastic waveguide. This model properly accounts for transducer dynamics, which is important when resonant transducers are employed, such as in this case. The model solves the modal amplitudes in the elastic waveguide of the propagating modes, given a voltage applied to the piezoelectric transducer.

Figure 5 depicts the model used in this case. The piezoelectric transducer is fixed under the head of the rail and is designed to preferentially excite modes with energy concentrated in the head of the rail as these modes are known to propagate long distances. From reference [13], the modal amplitudes of the propagating modes,

due to each of the transducer forces $\boldsymbol{F}_{t[n]}$, can be computed using:

$$\bar{\boldsymbol{\alpha}}_{\mathrm{Tx}}(\omega) = \sum_{n=1}^{N_t} ([\bar{\boldsymbol{\alpha}} e^{-j\boldsymbol{\kappa} z_f}]) \boldsymbol{N} \boldsymbol{F}_{t\,n}) \tag{9}$$

where $\bar{\boldsymbol{\alpha}}$ is an array of unit modal amplitudes resulting from unit forced responses computed using each waveguide degree of freedom in contact with the piezoelectric transducer and propagated to the front face of the transducer (a distance z_f). The array $\boldsymbol{F}_t$ effectively scales these unit responses by computing the actual forces acting on the waveguide due to the piezoelectric transducer, accounting for the voltage applied, the dynamics of the transducer and the stiffness of the waveguide to which the transducer is attached. Finally, the array $\boldsymbol{N}$ interpolates between the waveguide nodes and the transducer nodes which are not necessarily coincident. For more detail regarding this model, refer to [13]. It should be noted that $\bar{\boldsymbol{\alpha}}_{\mathrm{Tx}}(\omega)$ is a complex vector containing the modal amplitudes and phases of all excited propagating modes. Figure 6 depicts the modal amplitudes computed for a unit voltage at each frequency. The resonant nature of the transducer is evident with the peak amplitude at approximately $35kHz$.

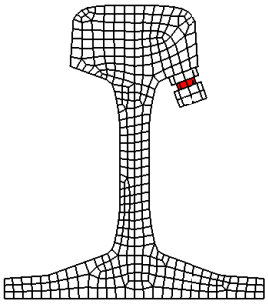

Figure 5: The hybrid SAFE-3D model for exciting guided waves in rail with a transducer.

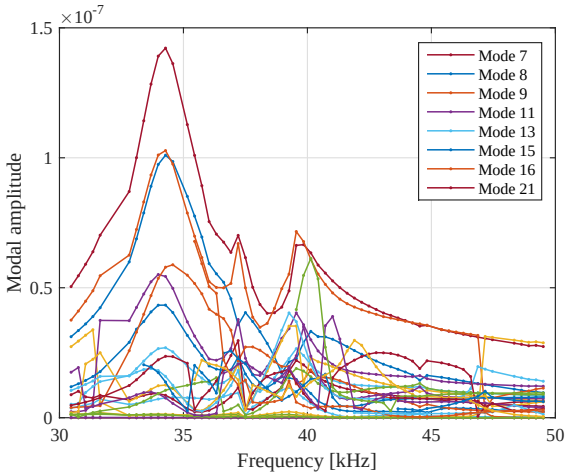

Figure 6: Modal amplitudes due to unit voltage excitation.

2.3. Hybrid SAFE-3D Model for Scattering from Discontinuities

This section presents the model used to simulate the scattering of propagating waves from discontinuities. As depicted in Figure 1 we specifically consider aluminothermic welds as reflectors in this case, but the procedure also applies to other discontinuities such as cracks or other defects that may result in reflections [3, 21].

The method proposed by Benmeddour et al. [20] is adopted and is presented in the notation proposed by the authors. The scenario considered is of an interior volume (I) containing the discontinuity, bounded by a semi-infinite incoming waveguide (L) with constant cross-section and an outgoing semi-infinite waveguide (R), as shown in Figure 7. The volume considered is, therefore, the union of these three volumes. Both the incoming waveguide and outgoing waveguides are modelled using SAFE, and the interior domain is modelled using solid finite elements. Enforcing continuity and equilibrium on the boundaries of L and R which intersect the interior volume, the reflected modal amplitudes $\bar{\boldsymbol{\alpha}}_L^-$ in the incoming waveguide, the transmitted modal amplitudes $\bar{\boldsymbol{\alpha}}_R^+$ in the outgoing waveguide and the internal displacements $\boldsymbol{U}_I$, due to incident modal amplitudes in the incoming waveguide $\bar{\boldsymbol{\alpha}}_L^+$, can be computed from the following linear system at each frequency considered [20]:

$$\begin{bmatrix} \boldsymbol{\psi}_L^{-T} & \mathbf{0} & \mathbf{0} \\ \mathbf{0} & \boldsymbol{I} & \mathbf{0} \\ \mathbf{0} & \mathbf{0} & \boldsymbol{\psi}_R^{+T} \end{bmatrix} \left(\begin{bmatrix} \boldsymbol{D}_{LL} & \boldsymbol{D}_{LI} & \boldsymbol{D}_{LR} \\ \boldsymbol{D}_{IL} & \boldsymbol{D}_{II} & \boldsymbol{D}_{IR} \\ \boldsymbol{D}_{RL} & \boldsymbol{D}_{RI} & \boldsymbol{D}_{RR} \end{bmatrix} \begin{bmatrix} \boldsymbol{\psi}_L^- & \mathbf{0} & \mathbf{0} \\ \mathbf{0} & \boldsymbol{I} & \mathbf{0} \\ \mathbf{0} & \mathbf{0} & \boldsymbol{\psi}_R^+ \end{bmatrix} - \begin{bmatrix} \boldsymbol{F}_L^- & \mathbf{0} & \mathbf{0} \\ \mathbf{0} & \mathbf{0} & \mathbf{0} \\ \mathbf{0} & \mathbf{0} & \boldsymbol{F}_R^+ \end{bmatrix} \right)$$
$$\times \begin{Bmatrix} \bar{\boldsymbol{\alpha}}_L^- \\ \boldsymbol{U}_I \\ \bar{\boldsymbol{\alpha}}_R^+ \end{Bmatrix} = - \begin{bmatrix} \boldsymbol{\psi}_L^{-T} & \mathbf{0} & \mathbf{0} \\ \mathbf{0} & \boldsymbol{I} & \mathbf{0} \\ \mathbf{0} & \mathbf{0} & \boldsymbol{\psi}_R^{+T} \end{bmatrix} \left(\begin{bmatrix} \boldsymbol{D}_{LL} & \boldsymbol{D}_{LI} & \boldsymbol{D}_{LR} \\ \boldsymbol{D}_{IL} & \boldsymbol{D}_{II} & \boldsymbol{D}_{IR} \\ \boldsymbol{D}_{RL} & \boldsymbol{D}_{RI} & \boldsymbol{D}_{RR} \end{bmatrix} \begin{bmatrix} \boldsymbol{\psi}_L^+ \\ \mathbf{0} \\ \mathbf{0} \end{bmatrix} - \begin{bmatrix} \boldsymbol{F}_L^+ \\ \mathbf{0} \\ \mathbf{0} \end{bmatrix} \right) \bar{\boldsymbol{\alpha}}_L^+ \tag{10}$$

where $\boldsymbol{\psi}_L$ and $\boldsymbol{\psi}_R$ are the mode shapes in the incoming and outgoing waveguides, respectively and the $(\cdot)^+$ and $(\cdot)^-$ are used to indicate the forward direction and backward directions, respectively. The partitioned dynamic stiffness matrix is denoted $\boldsymbol{D}$ and $\boldsymbol{F}$ represents the force modes.

In our case, the incident modal amplitudes are those excited by the transducer $\bar{\boldsymbol{\alpha}}_{\mathrm{Tx}}$, propagated to the weld. Since the system is linear, instead of exciting all modes simultaneously, we can consider each mode individually (excited by unit modal amplitude) and then later scale and superimpose the results. We will therefore introduce $\bar{\boldsymbol{R}}_{i,m}$ and $\bar{\boldsymbol{T}}_{i,m}$ as the arrays of unit reflection and transmission modal amplitudes corresponding with the modal amplitudes $\bar{\boldsymbol{\alpha}}^-_{L,i}$ and $\bar{\boldsymbol{\alpha}}^+_{R,i}$ corresponding to unit incident modal amplitude $\bar{\boldsymbol{\alpha}}^+_{L,m}$.

The reflection and transmission modal amplitudes when the target mode (mode 7) is incident to the weld, $\bar{\boldsymbol{R}}_{i,7}$ and $\bar{\boldsymbol{T}}_{i,7}$, are plotted in Figure 8. Only mode 7 was incident, but the other modes are reflected from the weld. This phenomenon is called mode coupling or mode conversion. Mode 7 transmitted strongly through the weld, but the other modes were also transmitted due to mode conversion. The calculation accuracy of the hybrid SAFE-3D model was verified using conservation of energy.

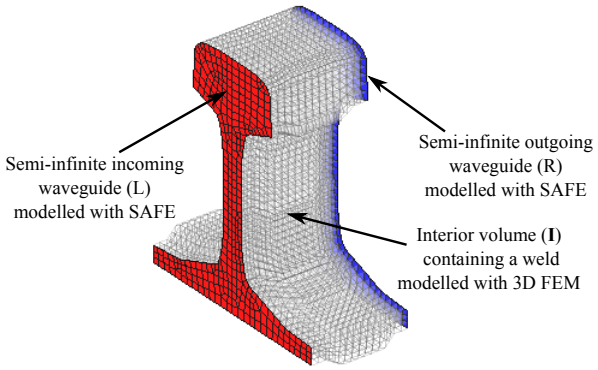

Figure 7: The hybrid SAFE-3D model of a rail section with a weld joint for guided wave scattering.

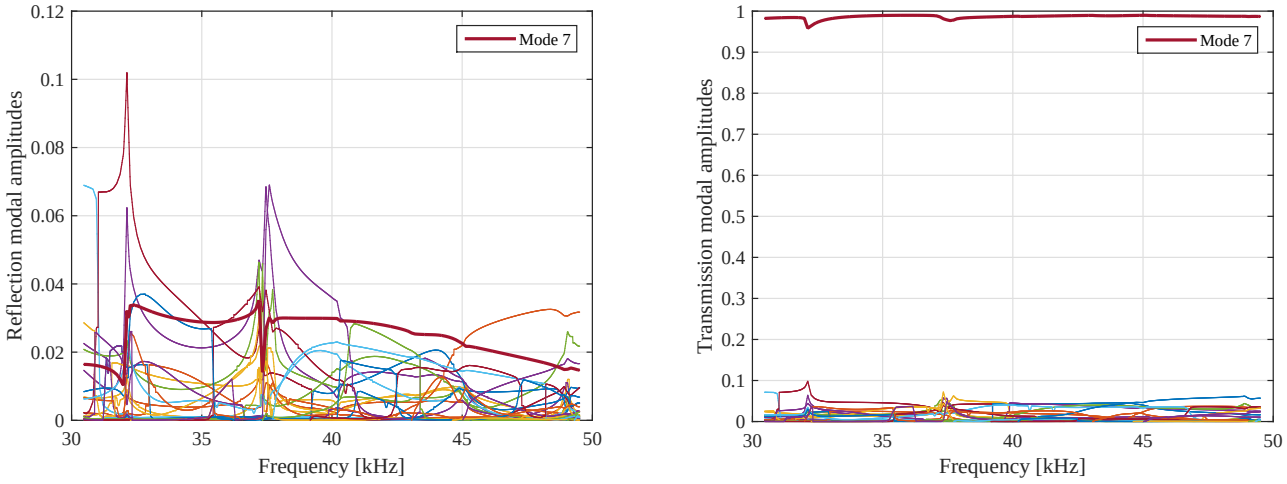

(a) Reflection modal amplitudes $\bar{\boldsymbol{R}}_{i,7}$.

(b) Transmission modal amplitudes $\bar{\boldsymbol{T}}_{i,7}$.

Figure 8: The reflection and transmission modal amplitudes for incident mode 7.

3. Guided Wave Measurements on a Rail Track

A simple GWU-based inspection of a rail track would involve a single transducer operating in pulse-echo mode. Such a measurement was performed on an operational heavy haul line, and the layout of this measurement

is illustrated in Figure 1. This line uses the UIC60 rail profile and was installed in 240m long sections joined together in the field by aluminothermic welding. The weld cap produced was ground off the top and sides of the railhead but remained around the remainder of the circumference of the rail. This change in cross-section of the rail causes a reflection of guided waves at the welds. The rail is clamped to concrete sleepers using steel clips, as shown in Figure 9. Polymer pads are compressed between the rail and the sleeper.

A piezoelectric transducer was attached under the head of the rail at a distance of approximately 78m from the nearest weld. The transducer was driven by a 17.5 cycle Hanning windowed tone burst voltage source with a centre frequency of 35kHz, as shown in Figure 10. The voltage applied to the piezoelectric element induced vibrations in the transducer, which in turn induced a guided wave field in the rail.

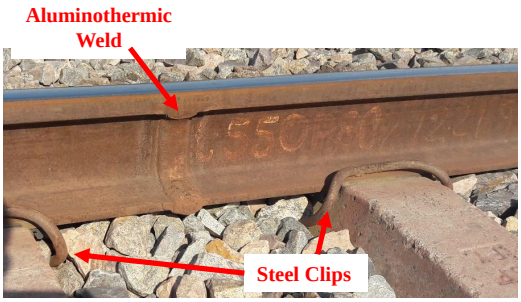

Figure 9: Steel clips in a rail with aluminothermic weld.

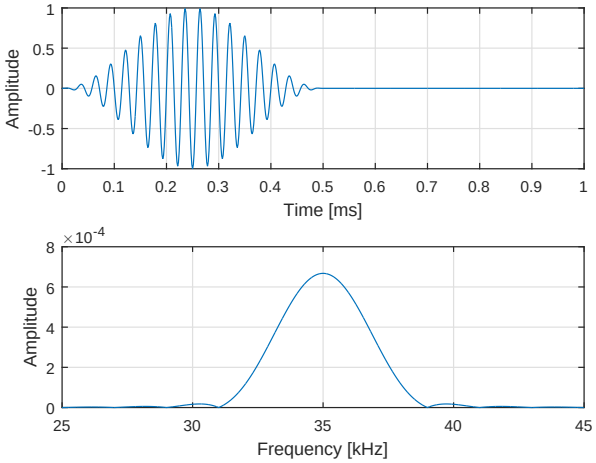

Figure 10: Excitation signal in time and frequency domains.

The transducer transmits guided waves in both directions along the rail. After excitation, the transducer was used to receive signals corresponding to the energy reflected from welds located on either side of the transducer. The measurement obtained from the field experiment which will be simulated in this paper is plotted in Figure 11a. The first part of the received signal is set to zero. This part of the signal includes the excitation signal and complex reflections of multiple modes from nearby reflectors such as the rail clips, that fortunately are not propagating modes. Hence, no attempt is made to simulate within this zone. The signal clearly shows the six weld reflections, with an exponential loss of energy from the weld closest to the transducer (weld A) to the furthest weld (weld F). Note that Weld F is located to the left of Weld D, but is not shown in Figure 1a. The time-domain signal shows that the propagating modes are highly dispersive. The frequency content of the measurement is shown in Figure 11b.

The possible modes of propagation captured in the signal were investigated by comparing times of arrival of different frequencies with estimates based on the distances to the welds and the group velocity predictions from a SAFE model. A short time Fourier Transform was applied to the measured time-domain signal to produce a time-frequency spectrogram, as shown in Figure 12. We then used the group velocities computed from the SAFE model to estimate the times of arrival for different combinations of modes propagating to and back from the welds. The predicted time of arrival as a function of frequency for a particular mode combination was then plotted as a curve on the spectrogram. If this curve coincided with a domain of higher energy in the spectrogram, then it was assumed that this mode combination was captured in the measurement. Figure 12 shows that there could be combinations of six different modes contributing to the field measurement. These mode shapes at two different frequencies are shown in Figure 13. The model of the rail profile included asymmetric rail wear, so the geometry of the rail was not symmetric. The wavenumber versus frequency curves does not cross in this situation. Instead, the curves may approach each other and then repel. The modes may, therefore, be numbered from the highest wavenumber to lowest wavenumber at a particular frequency. The mode shapes swap from one curve to the other in these mode repulsion regions [27]. The mode shape swapping between modes 15 and 16 and between modes 21 and 24 is evident in the figure.

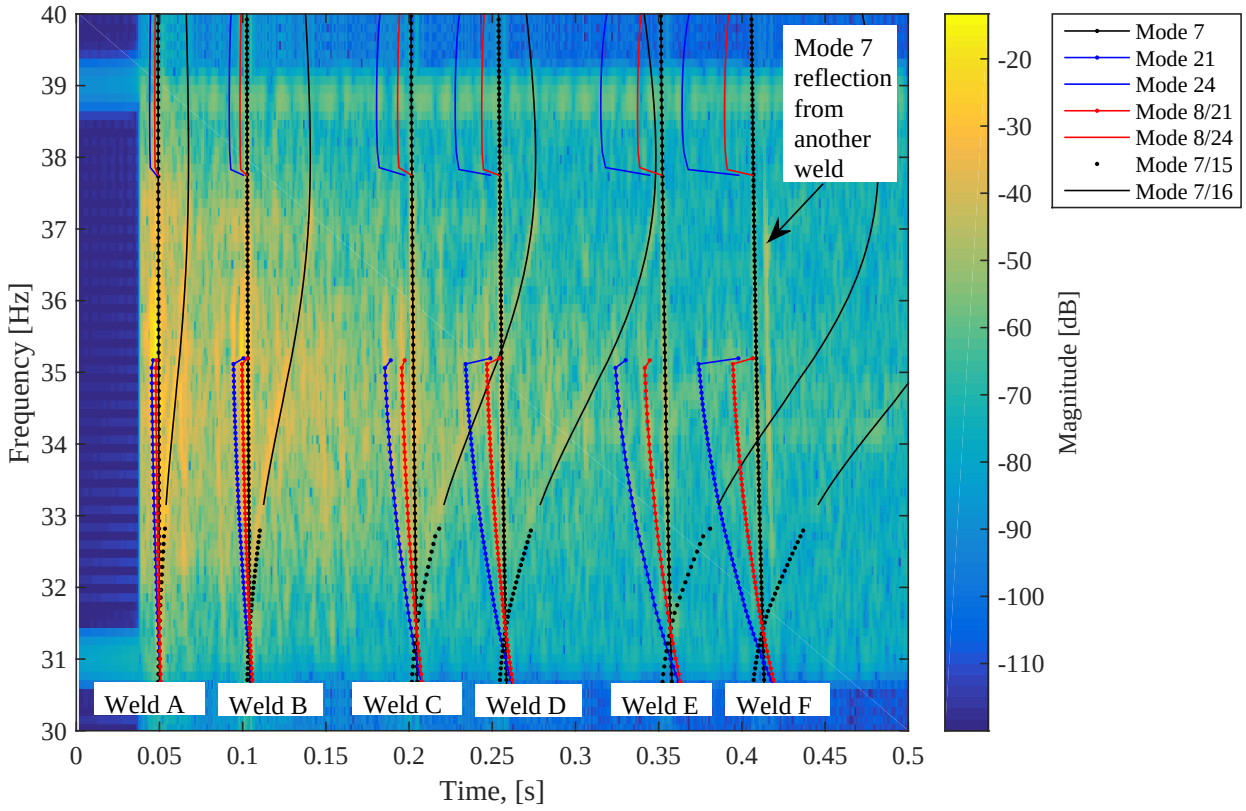

Figure 12: A spectrogram of the field measurement showing the times of arrival of the propagating modes.

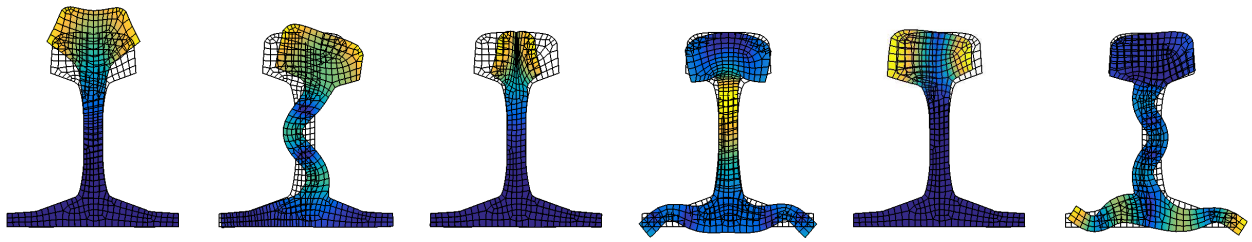

(a) Mode 7 at 32kHz. (b) Mode 8 at 32kHz. (c) Mode 15 at 32kHz. (d) Mode 16 at 32kHz. (e) Mode 21 at 32kHz. (f) Mode 24 at 32kHz.

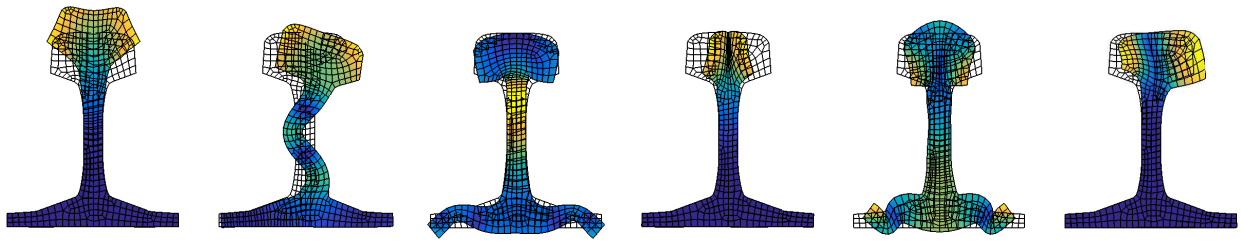

(g) Mode 7 at 39kHz. (h) Mode 8 at 39kHz. (i) Mode 15 at 39kHz. (j) Mode 16 at 39kHz. (k) Mode 21 at 39kHz. (l) Mode 24 at 39kHz.

Figure 13: The mode shapes of the propagating modes at 32kHz and 39kHz.

Mode 7 appears to propagate with low attenuation, has relatively little dispersion and is not involved in any mode repulsions, so the mode shape remains similar over the considered frequency range. This mode is

present in the spectrogram and propagates to a weld and reflects as mode 7 (incident and reflected modes the same). Also, this mode can reflect as a different mode (mode conversion). At low frequencies (below $33kHz$), mode 7 converts to the very dispersive mode 15 which switches its mode shape with mode 16 at $f > 33kHz$. These times of arrival are indicated on the spectrogram as curves denoted 7/15 and 7/16, and are referred to as coupled modes. Note that if mode 15 was transmitted and converted to mode 7 at a reflection, the time of arrival would be identical to that of mode 7 when transmitted and converted to mode 15. Another mode which propagates and reflects as the same mode is mode 21. However, it is noted that this mode only propagated well at $f < 35kHz$. Mode number 24, which becomes propagative at $f > 38kHz$, has a similar mode shape as mode 21 at the lower frequencies. Both modes appear to be non-propagative between $35khz < f < 38kHz$ as this is the frequency range where the modes swap and are highly dispersive. A similar behaviour is noticed in the coupling of modes 21 and 24 to mode 8.

Figure 14 plots the dispersion properties of the modes identified in the field experiment to illustrate the repulsion phenomenon. Two additional modes found to have a mode shape similar to mode 21 (at $f < 35kHz$) and mode 24 (at $f > 38kHz$) were identified and are also plotted. A frequency region where these two modes (22 and 23) switch their mode shapes with modes 21 and 24 is highlighted in Figure 14a, and clearly shown in Figure 14b where the repulsion behaviour is highlighted; the same mode shape switches from mode 21 to 22, then to 23 and finally to 24. The group velocity curves in Figure 14c further illustrates this phenomenon. In the frequencies where the repulsions happen, there exist some discontinuities as the mode shape switches from mode to mode. Furthermore, the repelling modes contain a large dispersion in that region. These discontinuities and large dispersion cause a frequency gap seen in the spectrogram (Figure 12) where the repelling modes do not show any energy.

Figures 15 and 16 interpret the modes identified from the spectrogram in the time domain signal for reflections from welds A and B, respectively. All modes identified can be seen in the time domain reflections for both welds. The reflections from weld A show an additional pulse of energy arriving just before the coupled modes 8/21 and 8/24, which appears to be less dispersive. It is speculated that this unidentified mode could be either mode 7 or 21 (or 24) coupled to some other mode with energy in the head. This pulse is not visible in the reflections from weld B, see Figure 16.

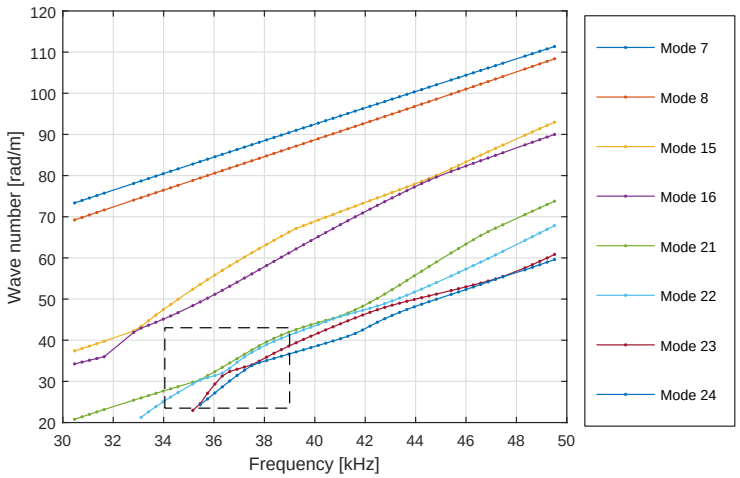

(a) Wavenumbers of the propagative modes with an example set of repelling modes highlighted.

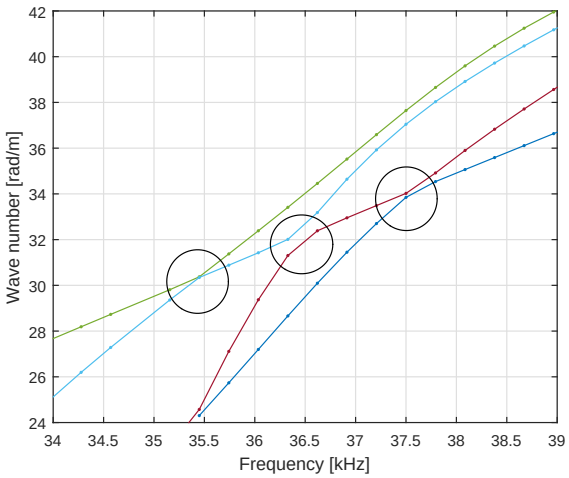

(b) An example set of repelling modes.

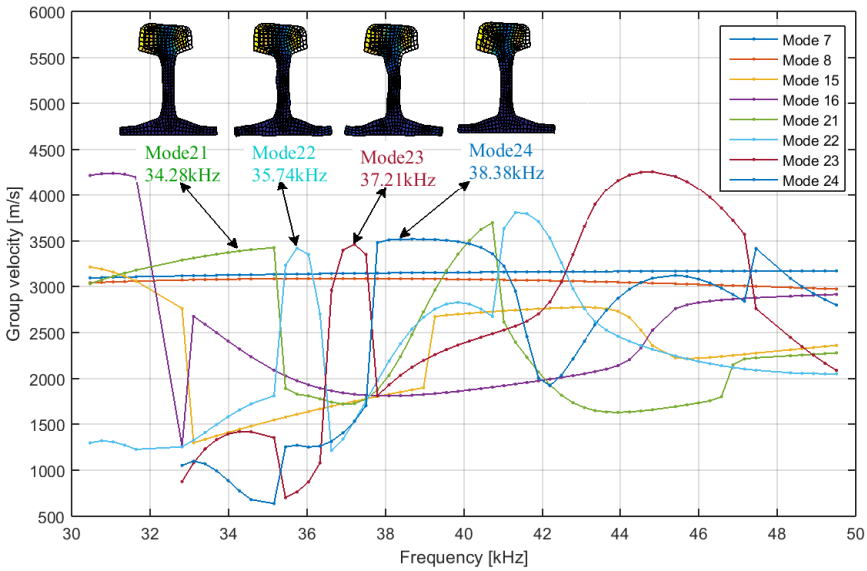

(c) The group velocity curves showing the mode shapes of the selected repelling set.

Figure 14: Dispersion properties of the modes identified in the field experiment.

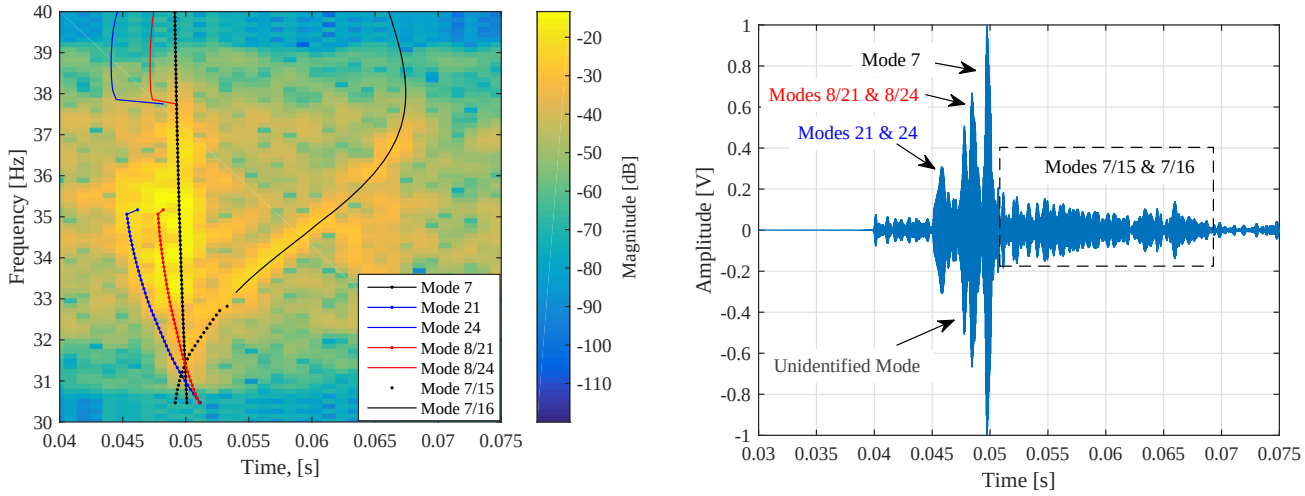

(a) Time-frequency spectrogram.

(b) Time domain signal.

Figure 15: Reflections from weld A.

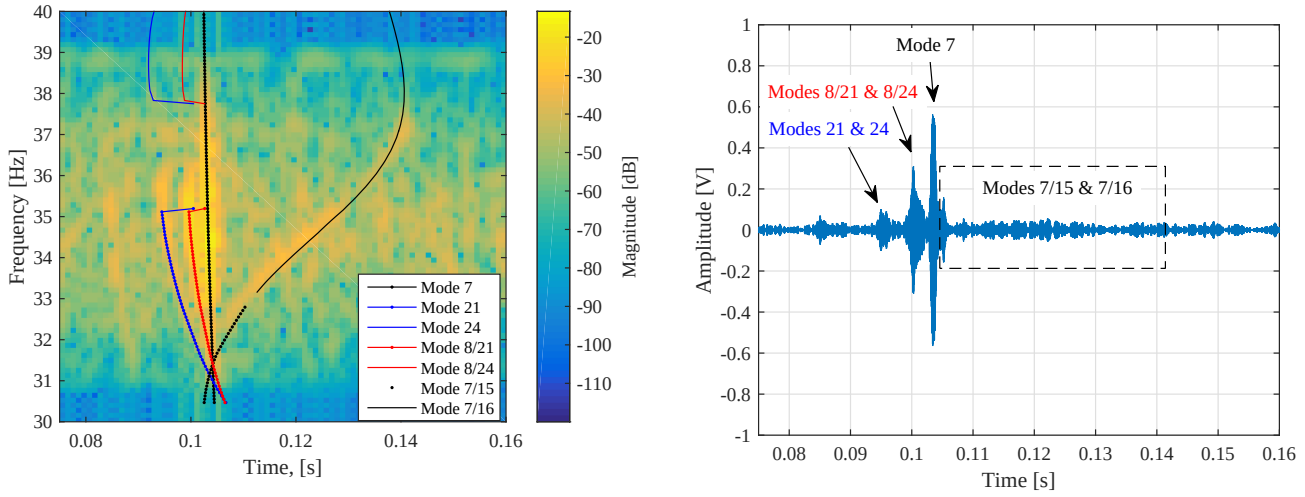

(a) Time-frequency spectrogram.

(b) Time domain signal.

Figure 16: Reflections from weld B.

The field measurement presented in this section is modelled and simulated in the next section.

4. Modelling Procedure

This section presents the proposed modelling framework illustrated in Figure 18 to simulate the experiment depicted in Figure 1, intending to reproduce the experimental results presented in the previous section, as closely as possible. Guided waves in rails are multi-modal, dispersive and can propagate hundreds (and sometimes thousands) of metres, which complicates their modelling. The model will consider the excitation of guided waves using a transducer, multi-modal propagation, including dispersion and attenuation effects and scattering of guided waves from welds. The reception of guided waves using a transducer is not modelled and is instead taken as the vertical displacement of a node in the railhead coincident with the centre node of the transducer

front face. There are also several real-world events that will not be considered, e.g. coherent noise resulting from reflections from features such as rail clips which secure the rail to the sleepers, and other similar effects.

Effects of EOCs are also not considered here. Liu et al. [2, 24] identified temperature as the main EOC influencing guided wave propagation in pipes. Temperature is known to have a significant effect on GWU propagation in rails [23], and methods to treat temperature have been proposed [31, 32]. Other EOCs which may be more challenging to simulate include the effects of passing trains and ballast conditions. These will be considered in future.

4.1. Computation of System Response

Guided wave propagation in welded rails is very complex due to the many possible reflections and transmissions caused by features in the rail. In this paper, we consider the direct reflection propagation paths. Illustrated in Figure 17, the guided waves induced by the transducer will propagate through to a specified weld position while transmitting through the prior welds. They will then reflect from that specified weld and transmit through the prior welds in the opposite direction, back to the transducer.

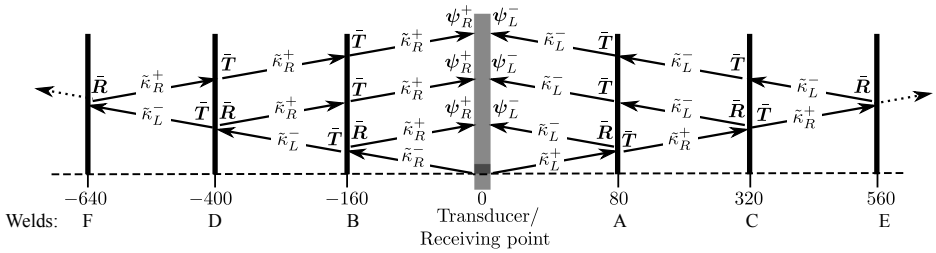

Figure 17: Direct reflection propagation paths.

The system response is most easily computed in the frequency domain, where the frequency response of multiple elements may be multiplied together. The response in the frequency domain due to propagating guided waves is given by:

$$U(z,\omega) = \sum_{i=1}^{I} \alpha_i(z,\omega)\boldsymbol{\psi}_i(\omega), \tag{11}$$

and is a sum of all the propagating mode shapes multiplied by their effective modal amplitudes computed at the distance where the response is sought. The mode shapes $\boldsymbol{\psi}$, are frequency-dependent, while the modal amplitudes $\boldsymbol{\alpha}$ depends on both the frequency ω and propagation distance z. The solution thus requires the computation of the modal amplitudes at the receiving location. In a constant cross-section waveguide without any discontinuities, the modal amplitudes $\boldsymbol{\alpha}$ at any distance z can easily be evaluated from the multiplication of the transducer modal amplitudes $\boldsymbol{\alpha}_{\mathrm{Tx}}$ with the exponential term $exp(-j\tilde{\boldsymbol{\kappa}}(\omega)z)$.

From Figure 17, the modal amplitudes of the received guided wave reflections from weld A, can be evaluated as:

$$\alpha_{\mathrm{A},i}(z=0) = \sum_{m=1}^{M} \alpha_{\mathrm{Tx},m} e^{-j\tilde{\kappa}^{+}_{L,m} z_{\mathrm{A}}} \bar{\boldsymbol{R}}_{im} e^{-j\tilde{\kappa}^{-}_{L,i}(-z_{\mathrm{A}})} \tag{12}$$

where $\bar{\boldsymbol{R}}_{im}$ is the I by M reflection matrix indicating the reflection coefficient of mode i for an incident mode m of unit modal amplitude and $\tilde{\boldsymbol{\kappa}}^{+}_{L}$ and $\tilde{\boldsymbol{\kappa}}^{-}_{L}$ are the forward and backward propagation wavenumbers for the incoming waveguide. Equation (12) gives the effective modal amplitudes of the received guided waves obtained by first propagating the guided waves excited by the transducer (with modal amplitudes of $\boldsymbol{\alpha}_{\mathrm{Tx}}$, Figure 19) forward to weld A (first exponential in Equation (12)). They are then reflected in the backward direction with $\bar{\boldsymbol{R}}_{im}$, whereafter they are propagated in the opposite direction from weld A back to the transducer (second exponential in Equation (12)). Finally, summing all the individual amplitudes of each reflected mode i resulting from the interaction of each mode m with the weld, $\alpha_{\mathrm{A},i}(z=0)$ is obtained. The response at the receiving point for reflections coming from weld A can then be obtained by substituting α_i with the modal amplitudes

in Equation (12) and $\boldsymbol{\psi_i}$ with the mode shapes for backward propagation on the incoming waveguide, $\boldsymbol{\psi}_L^-$, in Equation (11).

Equation (12) can be presented using vector and matrix multiplication notation as follows:

$$\{\boldsymbol{\alpha}_{\mathrm{A}}(z=0)\}^T = \left\{\{\boldsymbol{\alpha}_{\mathrm{Tx}}\} \circ \left\{e^{-j\tilde{\boldsymbol{\kappa}}_L^+ z_{\mathrm{A}}}\right\}\right\}^T \left[\bar{\boldsymbol{R}}\right] \circ \left\{e^{-j\tilde{\boldsymbol{\kappa}}_L^-(-z_{\mathrm{A}})}\right\}^T \tag{13}$$

where $(\circ)$ is the Hadamard element by element multiplication between vectors.

To compute the reflections coming from weld C, we consider the forward propagation to weld A, then transmission through A followed by forward propagation to weld C, and then the reflection from weld C followed by backward propagation to weld A, the transmission through weld A and finally the backward propagation of the modes back to the transducer location. The reflected modal amplitudes from weld C at the receiving point are thus given by:

$$\{\boldsymbol{\alpha}_{\mathrm{C}}(z=0)\}^T = \left\{\{\boldsymbol{\alpha}_{\mathrm{Tx}}\} \circ \left\{e^{-j\tilde{\boldsymbol{\kappa}}_L^+ z_{\mathrm{A}}}\right\}\right\}^T \left[\bar{\boldsymbol{T}}\right] \circ \left\{e^{-j\tilde{\boldsymbol{\kappa}}_R^+(z_{\mathrm{C}}-z_{\mathrm{A}})}\right\}^T \left[\bar{\boldsymbol{R}}\right] \circ \left\{e^{-j\tilde{\boldsymbol{\kappa}}_L^-(z_{\mathrm{A}}-z_{\mathrm{C}})}\right\}^T \left[\bar{\boldsymbol{T}}\right] \circ \left\{e^{-j\tilde{\boldsymbol{\kappa}}_L^-(-z_{\mathrm{A}})}\right\}^T \tag{14}$$

For reflections coming from the w^{th} weld, the guided waves will transmit forward and backward through the preceding $(\mathrm{w}-1)^{th}$ welds, and the modal amplitudes received will be given by:

$$\begin{aligned}\{\boldsymbol{\alpha}_{\mathrm{w}}(z=0)\}^T = \left\{\{\boldsymbol{\alpha}_{\mathrm{Tx}}\} \circ \left\{e^{-j\tilde{\boldsymbol{\kappa}}_L^+(z_1-z_0)}\right\}\right\}^T \left[\bar{\boldsymbol{T}}\right] \circ \ldots \circ \left\{e^{-j\tilde{\boldsymbol{\kappa}}_R^+(z_{i-1}-z_{i-2})}\right\} \bar{\boldsymbol{T}} \circ \left\{e^{-j\tilde{\boldsymbol{\kappa}}_R^+(z_i-z_{i-1})}\right\} \left[\bar{\boldsymbol{R}}\right] \\ \circ \left\{e^{-j\tilde{\boldsymbol{\kappa}}_L^-(z_{i-1}-z_i)}\right\} \left[\bar{\boldsymbol{T}}\right] \circ \ldots \circ \left\{e^{-j\tilde{\boldsymbol{\kappa}}_L^-(z_0-z_1)}\right\}\end{aligned} \tag{15}$$

where $\mathrm{w} = 1, 2, 3 \ldots \mathrm{W}$ indicate the welds $\mathrm{A}, \mathrm{C}, \mathrm{E} \ldots \mathrm{W}$.

The displacement response of the reflections coming from the w^{th} weld in the frequency domain is then:

$$U_{\mathrm{w}}(\omega) = \sum_{i=1}^{I} \alpha_{\mathrm{w},i} \boldsymbol{\psi}_{L,i}^- \tag{16}$$

The solutions for welds situated to the left of the transducer (i.e. welds B, D, F...) can be computed by employing positive/negative propagation wavenumbers at appropriate places in Equation (15), and positive propagation $\boldsymbol{\psi}_R^+$ in Equation (16).

The total displacement response in the frequency domain due to all the considered reflection paths is obtained by summing the individual weld responses:

$$U(\omega) = \sum_{\mathrm{w}=1}^{\mathrm{W}} U_{\mathrm{w}}(\omega) \tag{17}$$

and the time domain response may be computed as the inverse Fast Fourier Transform (IFFT) of the frequency response:

$$U(t) = ifft(U(\omega)). \tag{18}$$

The complex multiple reflection paths where guided waves can reflect back and forth between any two welds are not analysed in this paper as they are insignificant in the experiment which is simulated. The multiple reflection which will be expected to produce the largest signal is that between welds A and B, where excited guided waves propagate forward to weld A, then reflect and propagate backwards to weld B (assuming that the transducer does not influence the propagating waves, i.e. no scattering from the transducer) where the second reflection happens causing the waves to propagate forward again and back to the transducer. The signal received for this path was simulated, and as expected, the received reflection was insignificant compared to reflections from weld A. A check can also be performed by evaluating the modal amplitudes of the received reflections.

We demonstrate this for a single frequency (at $35kHz$) for mode 7, which is the strongly excited and the least attenuated mode. The guided wave properties for mode 7 at $35kHz$ are listed in Table 2 and used to evaluate the

received modal amplitudes for the direct reflection from weld A and the multiple reflection path between welds A and B. The received modal amplitude for the multiple reflection path is 1.17% that of the direct reflection from weld A. The multiple reflection would be expected at approximately $0.15s$, and the coherent noise (see Figure 10a) is significantly larger than the expected reflection. Therefore, multiple reflection paths are not expected to be identified in the measurement.

In situations involving geometries which reflect waves more strongly, it may be necessary to include multiple reflection paths.

Table 2: Guided wave properties of mode 7 at $35kHz$.

Property	Value
Real valued wavenumber, $real(\tilde{\kappa}_L^+)$	$82.81\,rad/m$
Attenuation $imag(\tilde{\kappa}_L^+)$	$2.46e-2\,dB/m$ $2.46e-2\,/-8.686=-0.0028\,rad/m$
Complex wavenumber, $\tilde{\kappa}_L^+=-\tilde{\kappa}_L^-=\tilde{\kappa}_R^+$	$82.81-0.0028j\,rad/m$
Reflection modal amplitude, $\bar{R}_{77}$ Magnitude of $\bar{R}_{77}$	$0.0199-0.0208j$ 0.0288
Received modal amplitude for the direct reflection from weld A, for $\alpha_{\mathrm{Tx}}=1$	$\alpha_{\mathrm{Tx}}e^{-j\tilde{\kappa}_L^+ z_{\mathrm{A}}}\bar{R}e^{-j\tilde{\kappa}_L^-(-z_{\mathrm{A}})}=0.0183$
Received modal amplitude for the multiple reflection between welds A and B, for $\alpha_{\mathrm{Tx}}=1$	$\alpha_{\mathrm{Tx}}e^{-j\tilde{\kappa}_L^+ z_{\mathrm{A}}}\bar{R}e^{-j\tilde{\kappa}_L^-(z_{\mathrm{B}}-z_{\mathrm{A}})}\bar{R}e^{-j\tilde{\kappa}_R^+(z_{\mathrm{B}})}=0.000213$

4.2. Modelling Framework

The simulation framework is detailed in Figure 18. The process starts by selecting an excitation signal $V(t)$. In this paper, $V(t)$ is selected as a 17.5 cycle Hanning windowed tone burst centred at $35kHz$ depicted in Figure 10, but is $0.5s$ in length to allow for reflections up to $700m$ away from the transducer to be captured. The signal is sampled at $500kHz$ and thus contain over 2^{16} points in the time domain. A unit voltage is selected, but since the system is linear, the response can be scaled appropriately to represent the actual voltage applied to the transducer. This long time signal $V(t)$ is converted to the frequency domain using a Fast Fourier Transform (FFT), leading to a frequency signal $V(\omega)$ with 2^{17} samples. Since it is impractical to solve the models at so many frequency points, a reduced vector of frequencies $\tilde{\omega}$ is selected covering the frequency range of interest, which is usually selected to be where the excitation signal $V(\omega)$ has at least 0.05% of the energy at the centre frequency of the tone burst. For this paper, the reduced frequency vector was selected to contain 56 points between $30kHz$ and $50kHz$, to allow for multiple analyses with different centre frequencies. However, following the proposed guideline to select the frequency range, the range between $30kHz$ and $40kHz$ would have been appropriate for the results shown in this paper.

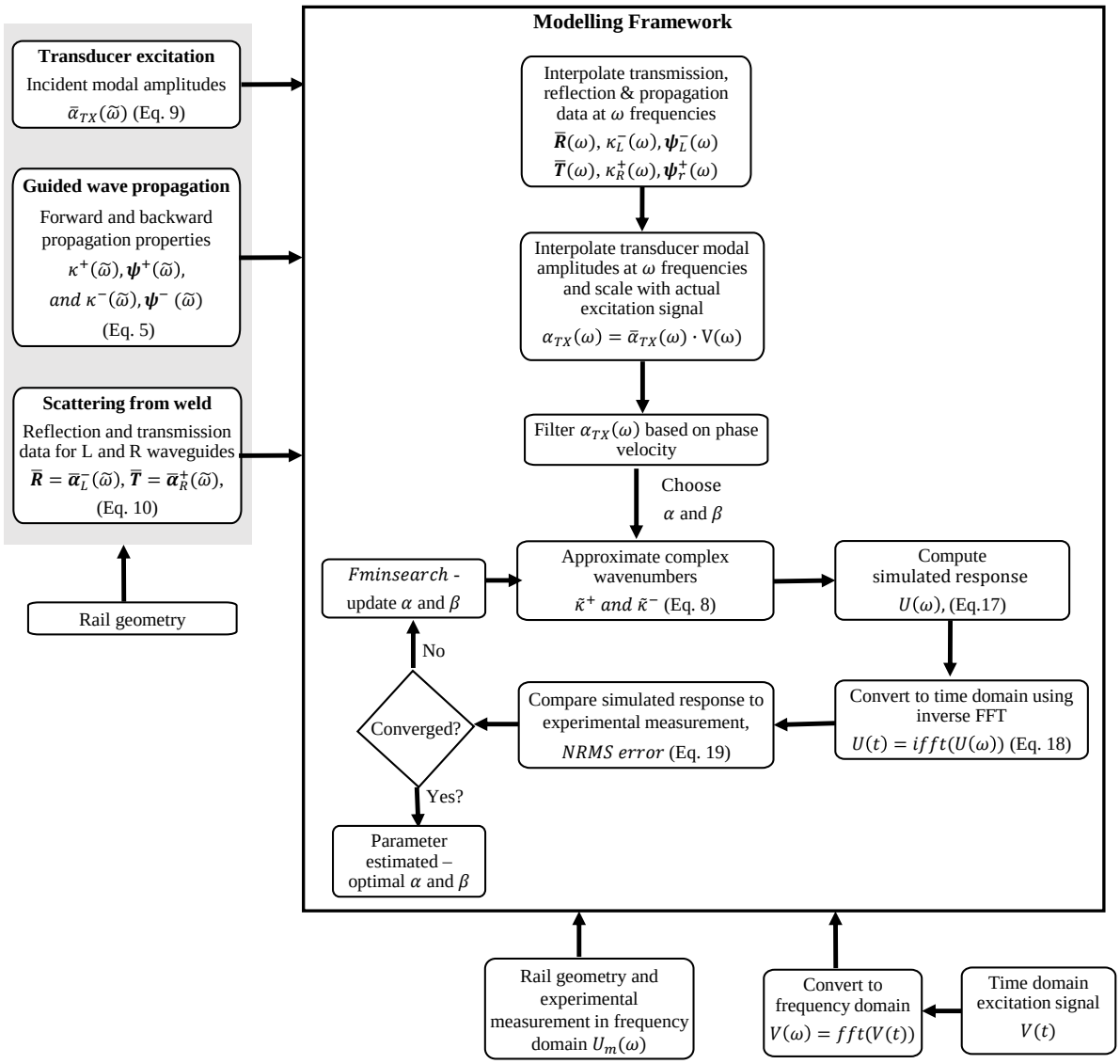

Figure 18: A procedure for modelling guided wave behaviour in discontinuous damped waveguides excited by transducers.

The SAFE problem, as well as transducer and weld scattering problems, are solved at $\tilde{\omega}$ frequencies as indicated in Sections 2.1, 2.2 and 2.3. The accuracy of the elements used in the three numerical models has been verified in earlier studies and presented in reference [33]. Both the transducer response as well as the reflections and transmissions from welds are solved with unit constant forces $\bar{V}(\tilde{\omega})$ and unit constant incident modal amplitudes $\bar{\boldsymbol{\alpha}}_{L}^{+}(\tilde{\omega})$, respectively. The results are stored in the computer and could later be used in the modelling framework for different analyses (i.e. different rail setups and different excitation signals) where the actual excitation signals will be employed to perform appropriate scaling of results. It is thus possible to re-use the stored data without extra computational effort.

4.2.1. Interpolation of Dispersion and Scattering Model Results

The first step in the modelling framework is to interpolate the wavenumbers $\boldsymbol{\kappa}^{+}(\tilde{\omega})$ and $\boldsymbol{\kappa}^{-}(\tilde{\omega})$ and associated mode shapes $\boldsymbol{\psi}^{+}(\tilde{\omega})$ and $\boldsymbol{\psi}^{-}(\tilde{\omega})$ from the undamped free vibration SAFE problem; and the reflection and transmission modal amplitudes $\bar{\boldsymbol{R}}$ and $\bar{\boldsymbol{T}}$ from the weld scattering problem between the reduced frequencies $\tilde{\omega}$ and the frequencies ω from the excitation voltage function. The interpolation of the mode shape vectors required the mode shapes for all the $\tilde{\omega}$ frequencies to have the same phase to avoid interpolation errors.

4.2.2. Interpolation, Scaling and Filtering of Transducer Model Results

After interpolating the modal amplitudes $\bar{\boldsymbol{\alpha}}_{\mathrm{Tx}}(\tilde{\omega})$ from the transducer problem (Figure 6) to the fine frequency discretization ω, the transducer modal amplitudes are scaled based on the selected voltage frequency function $V(\omega)$, to obtain $\boldsymbol{\alpha}_{\mathrm{Tx}}(\omega)$. To avoid unrealistic responses at cut-off frequencies, $\boldsymbol{\alpha}_{\mathrm{Tx}}(\omega)$ terms associated to phase velocities of $v_p > 10000m/s$ are removed [13]. Figure 19 shows the magnitude of the complex modal amplitudes excited by the transducer, scaled with the excitation voltage spectrum.

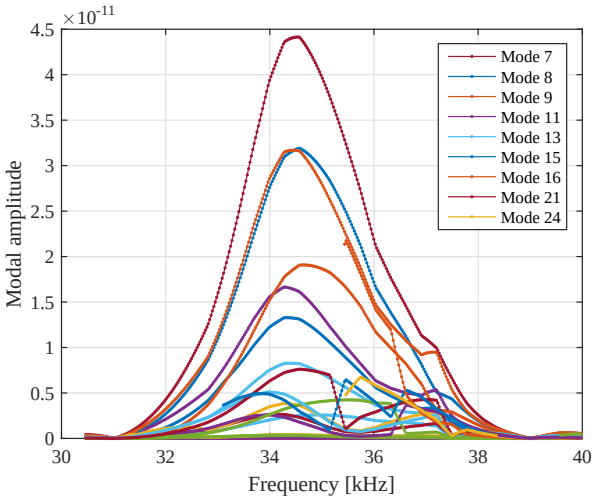

Figure 19: The magnitude of the complex modal amplitudes of the transducer scaled with the excitation voltage spectrum.

4.2.3. Estimation of Damping Parameters

After the interpolation and scaling of data, the next step in the modelling framework is to estimate appropriate damping parameters and use them to calculate the response signal $U(t)$ that closely fits the experimental measured $U_m(t)$. The damping parameters (β and c for hysteretic and viscous damping, respectively) are estimated using a model updating procedure which minimises the normalised root mean square ($NRMS$) error between the simulated response signal and the experimental measurement. The initial damping parameters, $(\beta_0, c_0) = (5e-5, 2e8)$ for model updating, were determined based on the experience of how the two damping models influence modal attenuation, after several trial and error investigations. Hysteretic damping adds some attenuation to all propagating modes, leading to an exponential decay of energy, whereas the viscous damping applied in the bottom of the rail attenuates modes with high energy in the foot.

After choosing the initial damping parameters, the complex wavenumbers for forward and backward propagation, $\tilde{\boldsymbol{\kappa}}^+$ and $\tilde{\boldsymbol{\kappa}}^-$ respectively, are approximated according to Section 2.1.2 at the analysis frequencies ω, and thereafter the response signal $U(\omega)$ is computed in the frequency domain using the procedure outlined in Section 4.1. The response is then transformed to the time domain response $U(t)$ using IFFT.

An unconstrained minimization algorithm from MATLAB, fminsearch, was adopted to solve the following optimization problem:

$$\text{Given damping parameters: } \beta \in \Re \text{ and } c \in \Re,$$

$$minimize: NRMS = \frac{\sum_{i=1}^{n}(U_i - U_{mi})^2/\bar{U}_{mi}}{n}, \tag{19}$$

where $U_{mi} = U_m(t)$, $\bar{U}_{mi} = \bar{U}_{mi}(t)$ and the simulated signal $U_i = U(t)$ is a function of the damping parameters β and c. $\bar{U}_{mi}$ is the exponential envelope fitted to the experimental measurement U_{mi} (see Figure 11a), used to normalise the errors and n is the number of time samples in the signals.

After multiple function evaluations, the optimization converged to the optimal parameters $(\beta, c) = (8.0499e-5, 2.4126e8)$. The surface of the $NRMS$ error was constructed to explore if other minima exist, and is plotted in Figure 20 with the contour plot indicating how the surface values change. The error surface shows one minimum in the explored domain, which coincides with the optimal solution (highlighted in red) from the optimization. This confirms that the optimization algorithm worked correctly and may be used in future.

These damping values were used to generate the results in the next section.

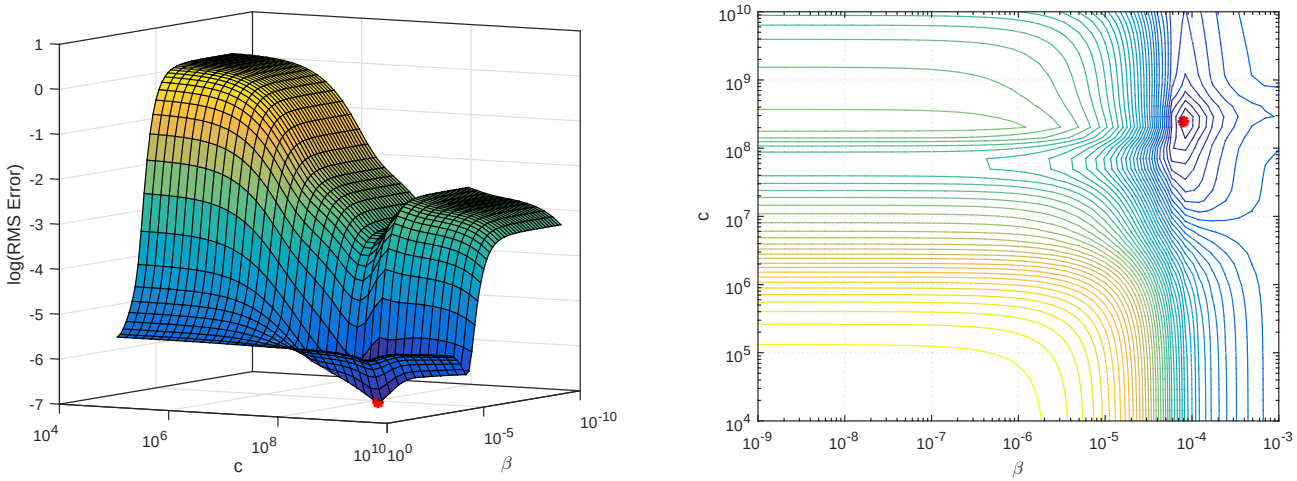

(a) RMS error surface.

(b) Surface contours.

Figure 20: $NRMS$ error surface for varying damping parameters, with the optimal solution highlighted in red.

5. Results

In order to demonstrate the performance of the modelling framework described in Section 4, the experiment depicted in Figure 1a is simulated with six identical welds included. The simulated time response is computed by taking the IFFT of Equation 17. The response was computed by considering all the propagating modes, using the steps described in Section 4. It is then shown that a similar result may be obtained by simulation with a smaller set of selected modes.

5.1. Simulation with all Propagating Modes

Firstly, the resultant simulated time-domain signal computed using all propagating modes and only direct reflection paths is considered. Figure 21 depicts the simulated time-domain response, normalised with respect to the maximum amplitude of the first weld reflection, together with the measured signal normalised in the same way. The reflections from the simulated welds are annotated and clearly visible. The most notable characteristics, namely times of arrival of the dominant reflections and attenuation, are accurately captured in the simulated result. This result is considered in more detail in Figure 22, which depicts the envelopes of the two signals and details around each weld reflection.

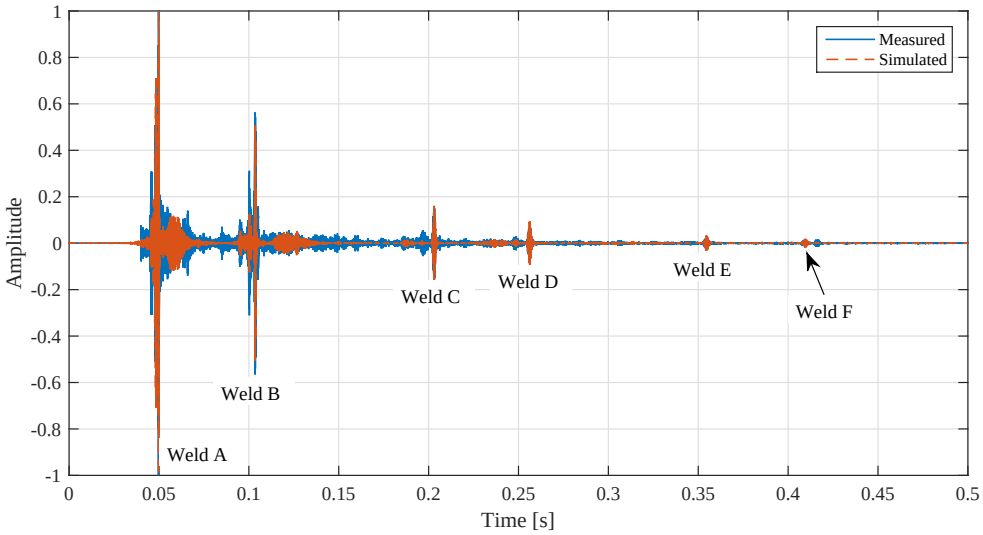

Figure 21: Simulated time domain signal compared to experimental measurement.

The behaviour of the uncoupled mode 7, which is the least dispersive mode and is known to propagate long distance in rail, is captured very accurately by the model, even though the amplitude at weld D, Figure 22e, is slightly overestimated. This could be due to slight variations in weld cap geometry which is not included in the model, i.e. the geometry of each weld in the model is identical. The attenuation of the coupled mode 8/21 and 8/24 seems to have been slightly overestimated based on the reflections from welds A to C, and the ratio between the simulated amplitude of mode 7 and mode 8/21 and 8/24 at weld D. The reflections from the uncoupled modes 21 and 24, and the very dispersive coupled reflections from 7/15 and 7/16 are relatively accurately captured. Figure 22g also shows a large reflection from a weld which was not included in the model.

The time-domain results presented in Figure 21 can be converted to the distance domain using a dispersion compensation procedure proposed by Wilcox [34]. The dispersion compensation procedure uses the dispersion characteristics of only one mode, and mode 7 was used in this case as it is the most prominent. The result in the distance domain is plotted in Figure 23. This figure shows that reflections from distant welds, over $640m$ from the transducer location, are still clearly visible. The regular (approximately 240m) spacing between welds results in the repeating pattern of reflections, apart from the identified reflection, which was not modelled. This reflection was found to be due to a weld approximately 100m to the right of weld E during a subsequent visual inspection.

The spectrogram of the simulated time signal is plotted in Figure 24, with detailed views presented in Figure 25. These spectrograms may be compared to the spectrograms of the experimental measurement shown in Section 3. It is noticed that the gaps due to mode repulsions are wider in the simulation, extending from $35.5kHz$ to $37.8kHz$ than in the experiment, which only ranges from $36.2kHz$ to $37.5kHz$.

The simulated spectrogram has more defined reflections when compared to the spectrograms of the experimental signals due to the absence of the coherent noise which is present in the measured results. The main reflection from mode 7 is clearly visible together with the uncoupled mode 21 and coupled mode 8/21. The other coupled modes with a similar mode shape to mode 21 (i.e. 22, 23 and 24) are not visible due to large dispersion in the region of repulsion and the lack of energy in the excitation signal above 38kHz. The coupled mode 7/16 is also very prominent in the spectrogram as is the case with the spectrogram of the measured signal.

Figure 25 highlights an additional reflection from an uncoupled mode 16, which was not identified in the experimental measurement. The presence of this mode in the simulated signal could imply that the mode was too strongly excited by the transducer model, or the damping applied to mode 16 was too low. Alternatively, this feature could be obscured in the spectrogram of the measured signal due to the presence of noise. Digital twins often miss features which are present in experimental measurements due to simplifications as we will

demonstrate in the next section. The results in this section, however, demonstrate that digital twins can also introduce features which are not apparent in the experimental measurements, either due to carelessness and poor modelling or by careful consideration of an analyst to highlight aspects hidden in the measured signals.

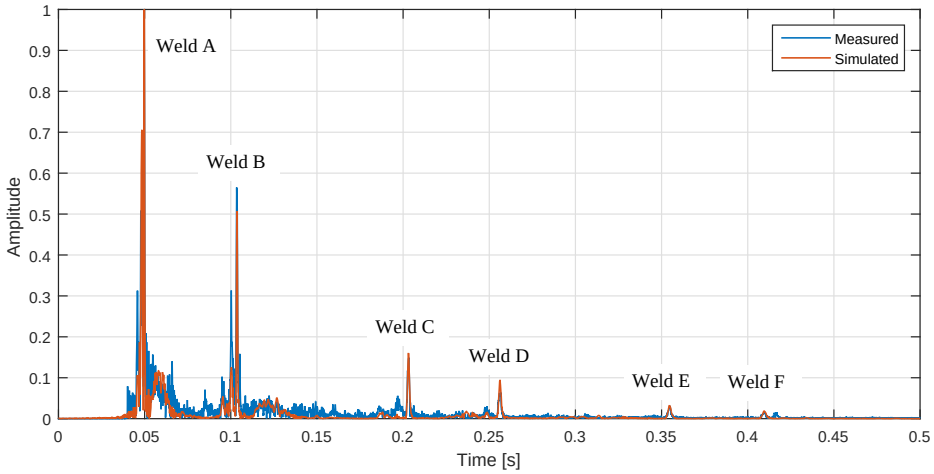

(a) All welds.

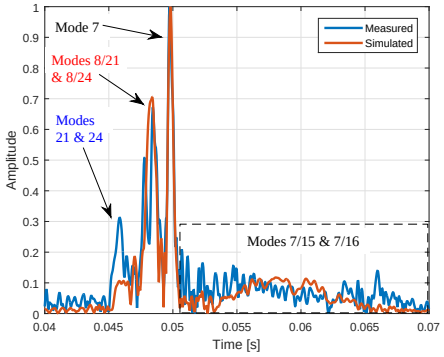

(b) Weld A.

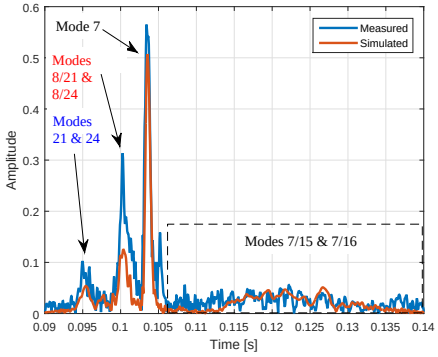

(c) Weld B.

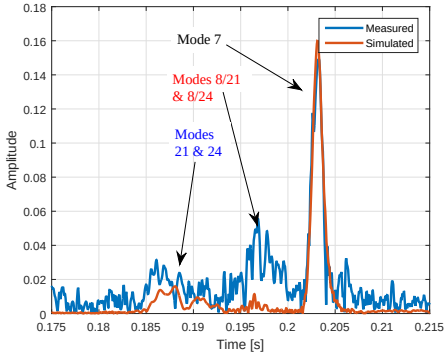

(d) Weld C.

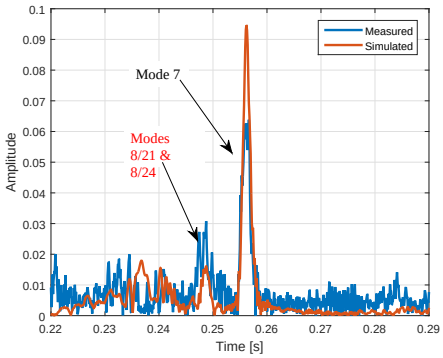

(e) Weld D.

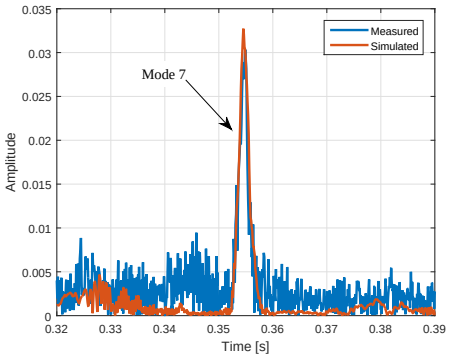

(f) Weld E.

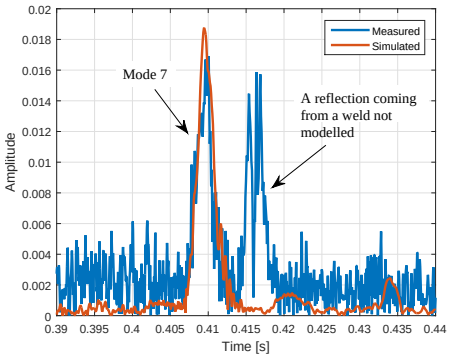

(g) Weld F.

Figure 22: Envelope comparison of the measured experiment and simulated time domain signals.

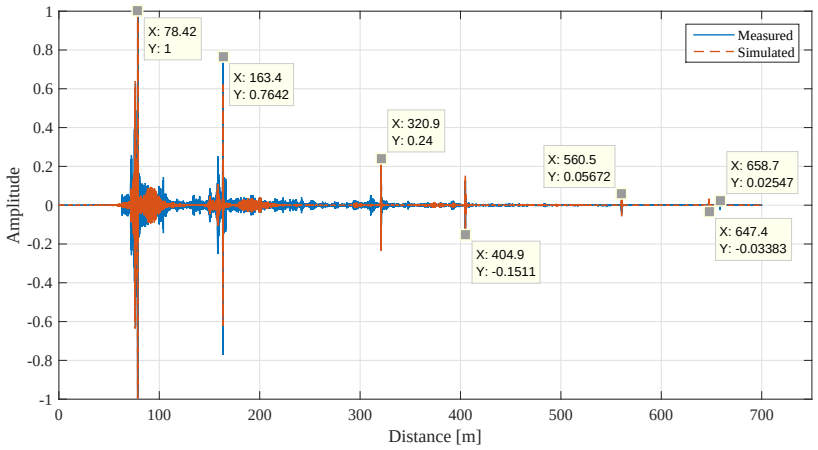

Figure 23: Simulated distance domain signal compared to the measured experimental signal.

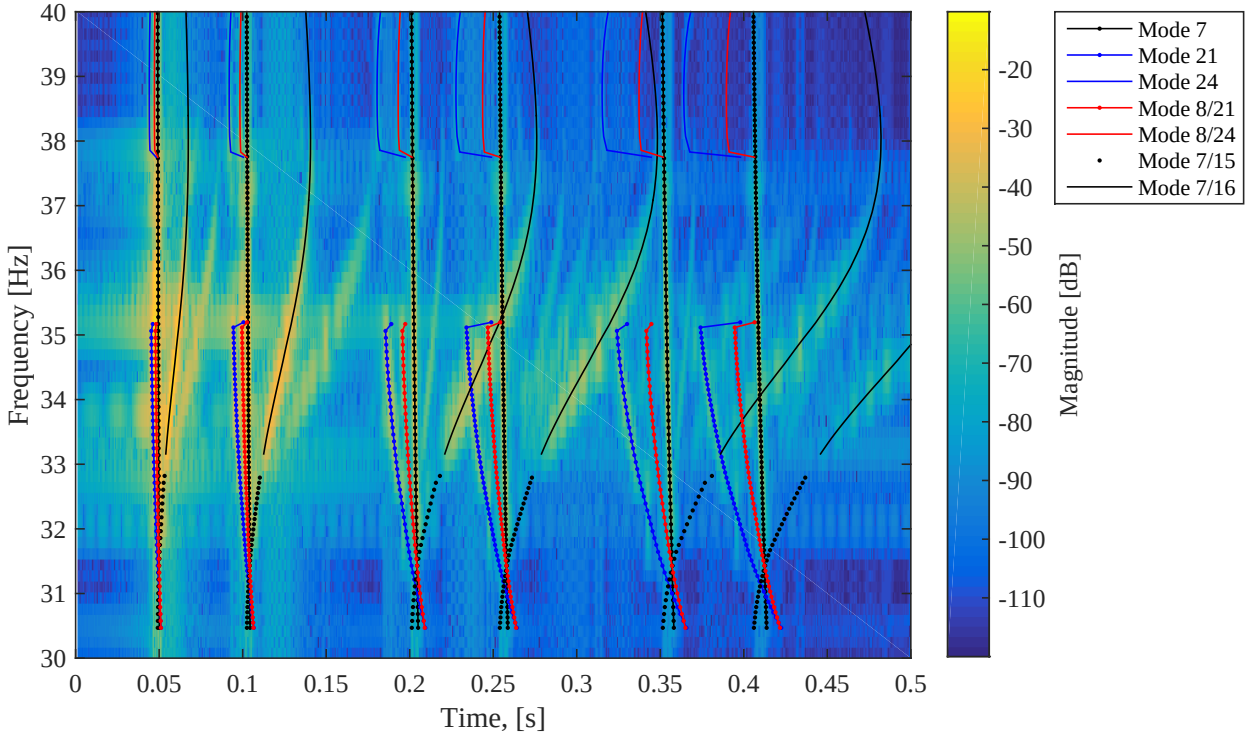

Figure 24: A spectrogram of the simulated measurement signal.

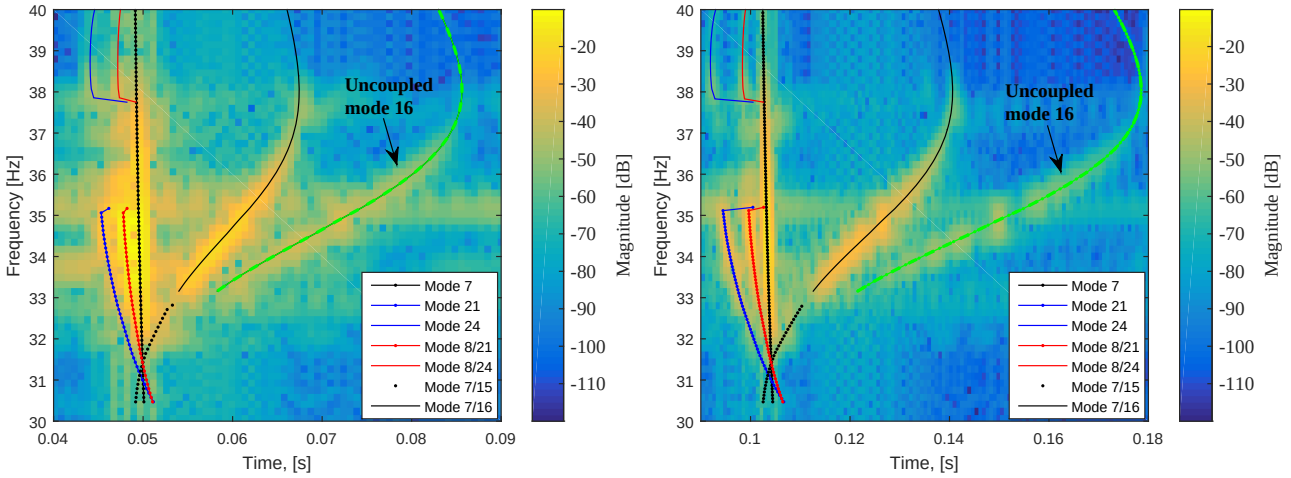

(a) Weld A.

(b) Weld B.

Figure 25: Spectrogram sections showing the reflection from welds A and B, respectively.

5.2. Simulation with Selected Modes

Instead of simulating the reflection signals using all 34 modes supported by the waveguide in the frequency range of interest, it is possible to construct the response by considering selected modes of interest only. To this end, the response is recomputed using only the six modes identified as contributing significantly to the response, namely modes 7, 8, 15, 16, 21 and 24. Figure 26a depicts the result computed using this reduced set of modes, compared to the result when all modes are used, with the residual (the difference between the signals) plotted in Figure 26b. The results are very similar since the modes neglected in the reduced problem are highly attenuated and thus do not contribute significantly to the response.

This simplified model could be used to reduce the problem complexity and computational effort, and make results easier to interpret. Figure 27 which is comparable to Figure 22b, shows the contribution of each selected mode in the total response. It is clear that modes 7, 21 and 16 were more strongly excited than the other modes. Furthermore, by considering each mode separately, it may be possible to apply different damping parameters to each mode in order to reproduce the experimental results better.

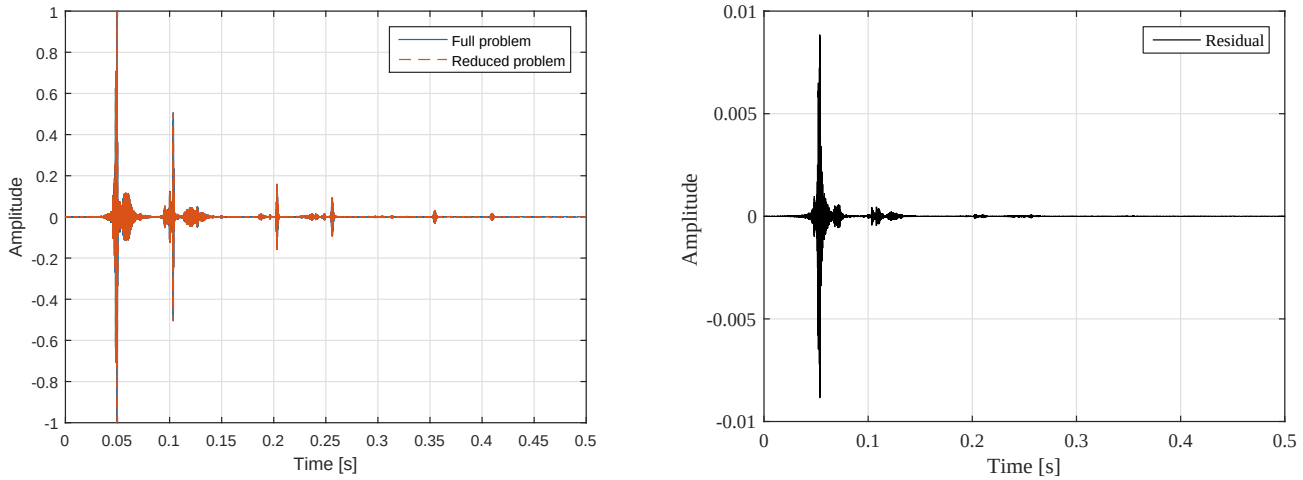

(a) Simulated signals.

(b) Residual signal.

Figure 26: The simulated time signal using reduced number of modes compared with the simulated experiment using all modes (Full problem).

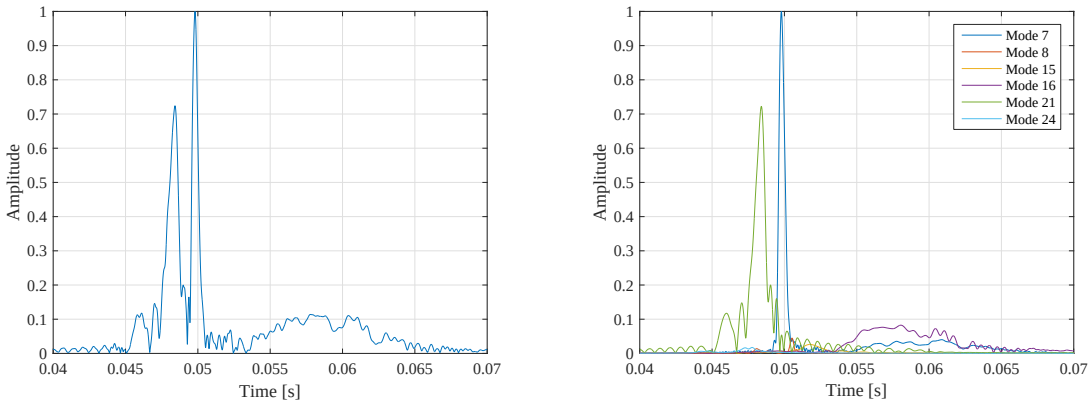

(a) Total response.

(b) Contribution of individual modes.

Figure 27: Reflections from the first weld simulated using the reduced number of modes.

6. Conclusion

The aim of this paper was to develop a modelling framework to simulate a realistic ultrasonic guided wave-based inspection of a rail track with multiple discontinuities. The simulation considered reflections from six identical welds located at various distances on either side of the excitation by a piezoelectric transducer. The effects of transducer dynamics as well as attenuation and dispersion, which are prominent due to the significant inspection range, were accounted for. Attenuation in the rail was approximated by determining the optimal hysteretic and viscous damping parameters using a model updating procedure. The excitation, scattering and propagation of guided waves were modelled using two different hybrid models and the conventional SAFE method, respectively. These three models were solved at discrete frequencies and results stored in a database. It was demonstrated how time domain voltage signals, applied to the piezoelectric transducer, can be converted to the frequency domain, and the database of model results can be interpolated at corresponding frequencies. Frequency domain results can then in turn be transformed back to the time domain. Scattering results computed for a specific discontinuity can be re-used, which allows for additional welds to be included or the positions of the welds in the rail to be rearranged without significant additional computational effort.

Overall good agreement between the simulated results and the experimental measurement was achieved. The times of arrival of the dominant reflections, the attenuation and the interaction of the multiple dispersive propagating modes were all accurately captured. Reflections from distant welds, over $640m$ from the transducer location, were clearly visible in the simulated and experimental signal. Slight overestimations of some reflection amplitudes could be attributed to slight variations in weld cap geometry, which is not modelled since all welds were assumed to be identical. A reflection from an uncoupled mode 16, which was not identified in the experimental measurement, was present in the simulation results. This could indicate that the mode was too strongly excited by the transducer model, or that the damping applied to mode 16 was not accurately estimated. Damping estimates could be improved by estimating parameters for each mode individually for example. Alternatively, this feature could be obscured in the spectrogram of the measured signal due to the presence of noise. This illustrates the point that a reliable numerical model can be useful when interpreting experimental results, since it has the potential to simulate features which are not apparent in the experiment.

The proposed physics-based framework can be used to efficiently investigate the effects of changes in parameters such as transducer geometry, or material property variations caused by temperature fluctuations. The framework could be used in future to set up a digital twin of a section of rail track, or in the development of a rail monitoring system by predicting reflections from defects which can be readily simulated but not measured.

References

[1] J. E. Michaels, T. E. Michaels, Damage Localization in Inhomogeneous Plates using a Sparse Array of Ultrasonic Transducers, in: Review of Quantitative Nondestructive Evaluation, Vol. 26, 2007, pp. 846–853.

[2] C. Liu, J. Dobson, P. Cawley, Practical Ultrasonic Damage Monitoring on Pipelines Using Component Analysis Methods, in: 19th World Conference on Non-Destructive Testing 2016, 2016, pp. 1–8.

[3] C. S. Long, P. W. Loveday, Prediction of guided wave scattering by defects in rails using numerical modelling, in: AIP Conference Proceedings, Vol. 1581 33, 2014, pp. 240–247. doi:10.1063/1.4864826.

[4] P. Loveday, D. Ramatlo, F. Burger, Monitoring of rail track using guided wave ultrasound, in: Proceedings of the 19th World Conference on Non Destructive Testing (WCNDT 2016), 2016, pp. 3341–3348.

[5] F. Burger, P. Loveday, Ultrasonic broken rail detector and rail condition monitor technology, in: Proceedings of the 11th International Heavy Haul Association Conference (IHHA 2017), no. September, 2017, pp. 275–280.

[6] F. C. R. Marques, A. Demma, Ultrasonic Guided Waves Evaluation of Trials for Pipeline Inspection, in: 17th World Conference on Nondestructive Testing, 2008.

[7] E. Leinov, M. J. Lowe, P. Cawley, Investigation of guided wave propagation and attenuation in pipe buried in sand, Journal of Sound and Vibration 347 (2015) 96–114. doi:10.1016/j.jsv.2015.02.036.

[8] I. Bartoli, F. Lanza Di Scalea, M. Fateh, E. Viola, Modeling guided wave propagation with application to the long-range defect detection in railroad tracks, NDT and E International 38 (5) (2005) 325–334. doi:10.1016/j.ndteint.2004.10.008.

[9] C. A. Leckey, K. R. Wheeler, V. N. Hafiychuk, H. Hafiychuk, H. Timuçin, Simulation of guided-wave ultrasound propagation in composite laminates: Benchmark comparisons of numerical codes and experiment, Ultrasonics (2018).

[10] M. Narayanan, A. Kumar, S. Thirunavukkarasu, C. Mukhopadhyay, Development of ultrasonic guided wave inspection methodology for steam generator tubes of prototype fast breeder reactor, Ultrasonics (2019).

[11] K. Jezzine, A. Lhemery, Simulation Of Guided Wave Inspection Based On The Rreciprocity Principle And The Semi-Analytical Finite Element Method, Review of Quantitative Nondestructive Evaluation 26 (2007) 39–46.

[12] P. W. Loveday, Analysis of piezoelectric ultrasonic transducers attached to waveguides using waveguide finite elements, IEEE Transactions on Ultrasonics, Ferroelectrics, and Frequency Control 54 (10) (2007) 2045–2051. doi:10.1109/TUFFC.2007.499.

[13] C. S. Long, P. W. Loveday, D. A. Ramatlo, E. V. Andhavarapu, Numerical verification of an efficient coupled SAFE-3D FE analysis for guided wave ultrasound excitation, Finite Elements in Analysis and Design 149 (2018) 45–56. doi:10.1016/j.finel.2018.05.001.

[14] D. A. Ramatlo, D. N. Wilke, P. W. Loveday, Development of an optimal piezoelectric transducer to excite guided waves in a rail web, NDT & E International 95 (2018) 72–81. doi:https://doi.org/10.1016/j.ndteint.2018.02.002.

[15] T. Hayashi, W. J. Song, J. L. Rose, Guided wave dispersion curves for a bar with an arbitrary cross-section, a rod and rail example, Ultrasonics 41 (3) (2003) 175–183. doi:10.1016/S0041-624X(03)00097-0.

[16] L. Gavric, Computation of propagative waves, Journal of Sound and Vibration 185 (3) (1995) 531–543.

[17] V. Baronian, A. E. Commission, K. Jezzine, A. E. Commission, S. Chatillon, A. E. Commission, Numerical methods for scattering by inhomogeneities in 3D elastic waveguides, 11th European Conference on Non-Destructive Testing (October) (2014).

[18] V. Baronian, K. Jezzine, Simulation of NDT Inspection in 3D Elastic Waveguide Involving Arbitrary Defect, 19th World Conference on Non-Destructive Testing (2016) 1–8.

[19] Ultrasonic testing with civa, accessed: 2020-04-03.
URL www.extende.com

[20] F. Benmeddour, F. Treyssède, L. Laguerre, Numerical modeling of guided wave interaction with non-axisymmetric cracks in elastic cylinders, International Journal of Solids and Structures 48 (5) (2011) 764–774. doi:10.1016/j.ijsolstr.2010.11.013.

[21] C. S. Long, P. W. Loveday, Analysis of guided wave scattering due to defects in rails using a hybrid FE-safe method, in: AIP Conference Proceedings, Vol. 1511, 2013, pp. 238–245. doi:10.1063/1.4789054.

[22] V. Baronian, A. E. Commission, A. E. Commission, K. Jezzine, A. E. Commission, Hybrid Safe/fe Simulation of Inspections of Elastic Waveguides Several Local Discontinuties Or Defects (August 2014) (2011). doi:10.1063/1.3591855.

[23] I. I. Setshedi, P. W. Loveday, C. S. Long, D. N. Wilke, Estimation of rail properties using semi-analytical finite element models and guided wave ultrasound measurements, Ultrasonics 96 (2019) 240–252. doi:10.1016/j.ultras.2018.12.015.

[24] C. Liu, J. Dobson, P. Cawley, Efficient generation of receiver operating characteristics for the evaluation of damage detection in practical structural health monitoring applications, Proceedings of the Royal Society A: Mathematical, Physical and Engineering Sciences 473 (2199) (2017) 1–26. doi:10.1098/rspa.2016.0736.

[25] R. Saracco, What would education be like in 2050? digital twins (February 2018).
URL https://cmte.ieee.org/futuredirections/2018/02/21/what-would-education-be-like-in-2050-digital-twins/

[26] V. Damljanović, R. L. Weaver, Forced response of a cylindrical waveguide with simulation of the wavenumber extraction problem, The Journal of the Acoustical Society of America 115 (4) (2004) 1582–1591. doi:10.1121/1.1675818.

[27] P. W. Loveday, C. S. Long, D. A. Ramatlo, Mode repulsion of ultrasonic guided waves in rails, Ultrasonics 84 (2018) 341–349. doi:10.1016/j.ultras.2017.11.014.

[28] J. Ryue, D. J. Thompson, P. R. White, D. R. Thompson, Decay rates of propagating waves in railway tracks at high frequencies, Journal of Sound and Vibration 320 (4-5) (2009) 955–976. doi:10.1016/j.jsv.2008.09.025.

[29] I. Bartoli, A. Marzani, F. Lanza di Scalea, E. Viola, Modeling wave propagation in damped waveguides of arbitrary cross-section, Journal of Sound and Vibration 295 (3-5) (2006) 685–707. doi:10.1016/j.jsv.2006.01.021.

[30] P. W. Loveday, Simulation of piezoelectric excitation of guided waves using waveguide finite elements, IEEE Transactions on Ultrasonics, Ferroelectrics, and Frequency Control 55 (9) (2008) 2038–2045.

[31] A. J. Croxford, J. Moll, P. D. Wilcox, J. E. Michaels, Efficient temperature compensation strategies for guided wave structural health monitoring, Ultrasonics 50 (4-5) (2010) 517–528. doi:10.1016/j.ultras.2009.11.002.

[32] J. B. Harley, J. M. Moura, Scale transform signal processing for optimal ultrasonic temperature compensation, IEEE Transactions on Ultrasonics, Ferroelectrics, and Frequency Control 59 (10) (2012) 2226–2236. doi:10.1109/TUFFC.2012.2448.

[33] E. Andhavarapu, P. W. Loveday, C. S. Long, P. S. Heyns, Accuracy of semi-analytical finite elements for modelling wave propagation in rails, in: Proc. Seventh South African Conference on Computational and Applied Mechanics (SACAM10), 2010.

[34] P. D. Wilcox, A Rapid Signal Processing Technique to Remove the Effect of Dispersion from Guided Wave Signals, IEEE Transactions on Ultrasonics, Ferroelectrics, and Frequency Control 50 (4) (2003) 419–427.

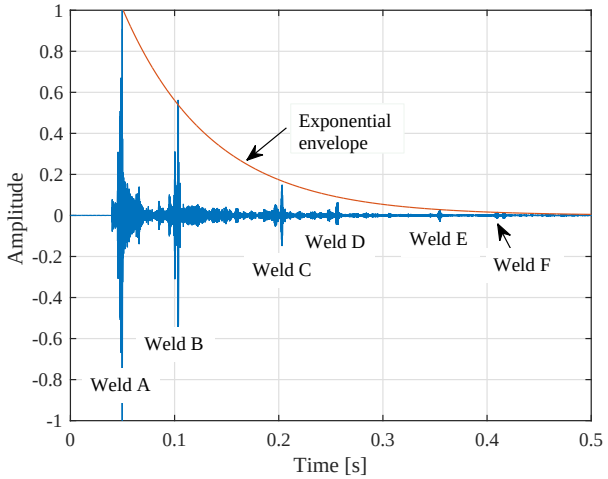

(a) Time domain signal.

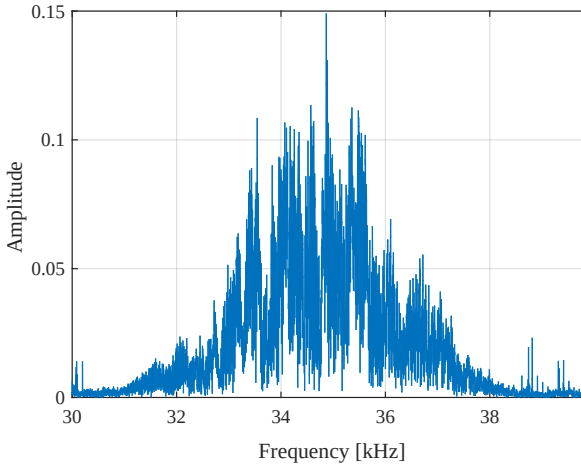

(b) Frequency domain signal.

Figure 11: The measurement obtained from the field experiment.